Monthly Notices
of the
ROYAL ASTRONOMICAL SOCIETY

MNRAS **486,** 1167–1191 (2019)
Advance Access publication 2019 January 22

doi:10.1093/mnras/stz217

The GALAH survey and *Gaia* DR2: dissecting the stellar disc's phase space by age, action, chemistry, and location

Joss Bland-Hawthorn [1,2,3]† Sanjib Sharma [1,2] Thor Tepper-Garcia [1,2] James Binney [4] Ken C. Freeman,[5] Michael R. Hayden,[1,2] Janez Kos,[1] Gayandhi M. De Silva,[1,6] Simon Ellis,[6] Geraint F. Lewis,[1] Martin Asplund,[2,5] Sven Buder [7,8]‡ Andrew R. Casey [9,10] Valentina D'Orazi,[11] Ly Duong,[5] Shourya Khanna,[1,2] Jane Lin,[5] Karin Lind,[7,12] Sarah L. Martell [2,13] Melissa K. Ness,[14,15] Jeffrey D. Simpson,[13] Daniel B. Zucker,[6] Tomaž Zwitter [16] Prajwal R. Kafle,[17] Alice C. Quillen [18] Yuan-Sen Ting,[19,20,21] Rosemary F. G. Wyse[22] and the GALAH team

Affiliations are listed at the end of the paper

Accepted 2019 January 16. Received 2019 January 15; in original form 2018 September 7

ABSTRACT

We use the second data releases of the European Space Agency *Gaia* astrometric survey and the high-resolution Galactic Archaeology with HERMES (GALAH) spectroscopic survey to analyse the structure of our Galaxy's disc components. With GALAH, we separate the α-rich and α-poor discs (with respect to Fe), which are superposed in both position and velocity space, and examine their distributions in action space. We study the distribution of stars in the zV_z phase plane, for both V_ϕ and V_R, and recover the remarkable 'phase spiral' discovered by *Gaia*. We identify the anticipated quadrupole signature in zV_z of a tilted velocity ellipsoid for stars above and below the Galactic plane. By connecting our work with earlier studies, we show that the phase spiral is likely to extend well beyond the narrow solar neighbourhood cylinder in which it was found. The phase spiral is a signature of corrugated waves that propagate through the disc, and the associated non-equilibrium phase mixing. The radially asymmetric distribution of stars involved in the phase spiral reveals that the corrugation, which is mostly confined to the α-poor disc, grows in z-amplitude with increasing radius. We present new simulations of tidal disturbance of the Galactic disc by the Sagittarius (Sgr) dwarf. The effect on the zV_z phase plane lasts $\gtrsim$2 Gyr, but a subsequent disc crossing wipes out the coherent structure. We find that the phase spiral was excited $\lesssim$0.5 Gyr ago by an object like Sgr with total mass $\sim 3 \times 10^{10}\,M_\odot$ (stripped down from $\sim 5 \times 10^{10}\,M_\odot$ when it first entered the halo) passing through the plane.

Key words: astrometry – proper motions – stars: kinematics and dynamics – Galaxy: disc, evolution, structure.

1 INTRODUCTION

The European Space Agency (ESA) *Gaia* astrometric mission (Perryman et al. 2001; Prusti et al. 2016) has been eagerly anticipated for many years by the stellar and Galactic communities and the early results have not disappointed (DR2: Gaia Collaboration et al. 2018b). Wide-field stellar surveys across the Galaxy are fundamental to astrophysics because there are important measurements that can only be made in the near field. The remarkable precision of measured stellar parameters by *Gaia* after only two years of observations has triggered a flurry of new discoveries and new fields of study (e.g. Antoja et al. 2018; Gaia Collaboration et al. 2018a,c,d). Complementary spectroscopic surveys – RAVE

⋆ E-mail: jbh@physics.usyd.edu.au
† Miller Professor
‡ Fellow

(Steinmetz et al. 2006), APOGEE (Majewski et al. 2017), *Gaia*-ESO (Gilmore et al. 2012), LAMOST (Deng et al. 2012) – and are now able to exploit the overlap of targets with *Gaia* DR2 – this is the golden age of Galactic archaeology (Freeman & Bland-Hawthorn 2002).

Our focus here is on the synergy between *Gaia* and the Galactic Archaeology with HERMES (GALAH)[1] survey based at the Anglo-Australian Telescope (AAT) in Australia. This survey brings a unique perspective to Galactic archaeology by measuring accurate radial velocities and up to 30 elemental abundances for about a million stars (De Silva et al. 2015; Martell et al. 2017). The HERMES (High Efficiency and Resolution Multi-Element Spectrograph) instrument was designed and optimized for the GALAH survey specifically for the pursuit of Galactic archaeology (Freeman & Bland-Hawthorn 2008; Barden et al. 2010). The GALAH selection criteria were designed to be as simple as possible to avoid problems that adversely affect earlier surveys (Sharma et al. 2011). The primary selection is based on a magnitude range of $12 < V < 14$ and a cut in Galactic latitude, $|b| > 10$ deg. Thus, GALAH probes mainly the thin and thick discs of the Galaxy. The impact of *Gaia* was a key consideration from the outset, particularly with regard to choosing a bright limiting magnitude to ensure good distances for all stars.

The second GALAH data release (GALAH DR2) features stellar parameters, radial velocities, and up to 23 elemental abundances for 342 682 stars (Buder et al. 2018). All of these stars have complementary data from the *Gaia* DR2 data archive. GALAH's high-quality radial velocities, with mean errors of 0.1–0.2 km s^{-1} (Zwitter et al. 2018), are more accurate than the *Gaia* radial velocities, but comparable to or better than typical transverse velocities derived from the proper motions (Gaia Collaboration et al. 2018b). The GALAH-*Gaia* synergy[2] is particularly strong for local dwarfs that dominate the survey within about 1 kpc. We exploit this advantage in this study.

A major topic is the remarkable discovery of a phase-space signal in the local stellar disc by the *Gaia* team (Antoja et al. 2018). In a volume element defined by $(\Delta R, \Delta\phi, \Delta z) = (\pm 0.1, \pm 0.1, \pm 1)$ kpc^3 centred on the Sun, Antoja et al. (2018) detect a coherent spiral pattern in the space spanned by z and V_z. This phenomenon is indicative of a system that is settling from a mildly disturbed state to a stationary configuration (Lynden-Bell 1967) through the process of phase mixing (e.g. Binney & Tremaine 2008, section 4.10.2).

In Section 2, we establish notation and define the required coordinate systems. In Section 3, we characterize the GALAH survey and use it to understand better the gross structure of the Galaxy's discs. In Section 4, we analyse the phase spiral in detail using data from *Gaia* and GALAH taking advantage of the insights provided by angle-action coordinates. In Section 5, we present a novel manifestation of the tilt of the velocity ellipsoid as one moves away from the plane, and discuss the relation of the spirals seen in V_R and V_ϕ. In Section 6, some dynamical implications are considered prior to a search, in Section 7, for the phase spiral signal in N-body simulations of Sgr impacting the Galactic disc. Section 8 sums up and provides some pointers to future work.

[1] https://galah-survey.org/

[2] The power of this synergy is demonstrated by Kos et al. (2018a) who reveal that four well-known NGC 'open clusters' first identified in 1888 are projections and not physical systems. This requires the modulus of the velocity *vector* to be measured to better than 1 km s^{-1}.

2 COORDINATES

2.1 Terminology

Since the seminal work of Gilmore & Reid (1983), we have become accustomed to the idea that the Galaxy's disc comprises two components. Traditionally, these have been called the thin and the thick discs because Gilmore & Reid (1983) distinguished them by their contrasting vertical density profiles. In the last few decades, it has become clear that this terminology is unfortunate because the real dichotomy is between stars that are poor and rich in α-chain elements (O, Ne, Mg, Si, S, Ar, Ca, and Ti) with respect to iron.

Fuhrmann (1998) first noted in a survey of local F and G stars that there are two distinct populations characterized by high and low [Mg/Fe] abundances, and these are associated with the geometrically thick and thin discs, respectively. Many subsequent papers provided overwhelming evidence in support of this picture, most notably Bensby, Feltzing & Lundström (2003) and Bensby, Feltzing & Oey (2014) with follow-up studies of more elements at higher sensitivity. Bensby et al. (2011) first suggested a shorter scale length for the α-rich disc compared to the dominant α-poor disc that was confirmed by the APOGEE survey (Bovy 2015; Hayden et al. 2015). In recent years, this chemical distinction has been further emphasized by enhanced C/N in the older α-rich population, presumably due to the effects of dredge-up in old turn-off dwarfs and giants (Masseron & Gilmore 2015; Hawkins et al. 2015).

Chemistry always provides a firmer foundation for galaxy dissection than kinematics or spatial distributions because a star's chemical composition is invariant even as its orbit evolves. (There are exceptions to every rule, e.g. diffusion in giants can lead to different element ratios.) Moreover, the classical thin and thick discs are understood to overlap extensively in both configuration and velocity space so, in much of phase space, stars cannot be assigned to one disc or the other if only phase-space coordinates are known. Hence, dissection by chemistry is the preferred option.

As the number of stars with good spectra has grown, it has become clear that α-rich stars form a structure that is quite different from that formed by α-poor stars. Fig. 1 summarizes our current understanding of the Galaxy's discs. A disc comprising α-rich stars extends out to about the solar radius, having a scale height of order 1 kpc. A disc comprising α-poor stars extends beyond the solar radius. Out to that radius, it has a scale height of order 0.3 kpc but further out it flares, so at large radii α-poor stars can be found far from the plane.

In view of this picture, we shall refer to the α-poor and α-rich discs rather than to the thin and thick discs, consistent with the language used in the earlier papers cited above. Looking forwards, however, an improved nomenclature needs to recognize stellar populations that are even more depleted in [α/Fe] at all [Fe/H] than the inconveniently labelled α-poor disc. This realization dates back to at least Russell & Dopita (1992) in a seminal study of stellar abundances in the Magellanic Clouds.

Hasselquist et al. (2017) and Hasselquist et al. (2019, submitted) compile updated abundance data and show that there are *three* [α/Fe] sequences in the ([Fe/H], [α/Fe]) plane where the lowest [α/Fe] sequence arises from the accretion of massive dwarfs. A better naming convention, suggested by L. E. Hernquist in discussions with the GALAH team, is as follows: (i) α_+ for the [α/Fe]-rich sequence, (ii) α_o for the confusingly named [α/Fe]-poor sequence, and (iii) α_- for the newly established lower sequence. The compact notation refers to the stellar populations and is not specific to a

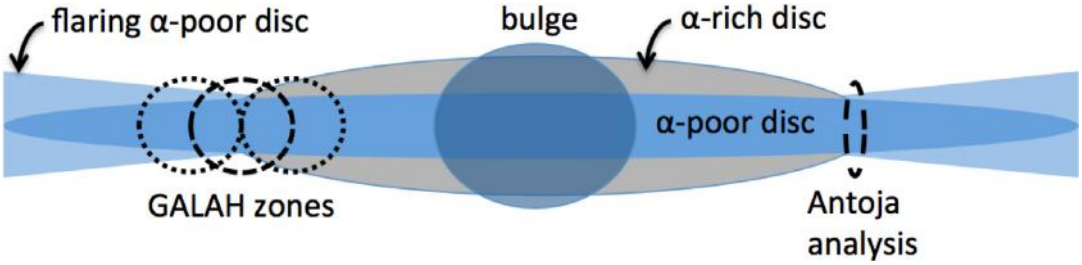

Figure 1. Schematic diagram of the modern interpretation of the disc structure (e.g. Hayden et al. 2015). The α-rich, inner thick disc has a shorter scale length than the α-poor inner thin disc and terminates near the Solar Circle. Here, the α-poor disc takes over and begins to flare at larger radii. It is appropriate now to speak of the α-rich and α-poor discs (relative to Fe) rather than the thick and thin discs. The thin vertical ellipse shows the extent of the Antoja et al. (2018) *Gaia* analysis. The large dashed and dotted circles show the domain our analysis; GALAH's low-latitude limit ($|b| > 10^\circ$) is not shown. Both the *Gaia* and GALAH studies were performed in the solar neighbourhood. Anywhere in the Galaxy, the stellar metallicity [Fe/H] declines with both R and z.

structural component. We illustrate the 'α notation' in a later figure (Fig. 21) and propose to use this language in subsequent GALAH papers.

2.2 Reference frame

We employ right-handed frames of reference for both the heliocentric and Galactocentric systems. In the heliocentric system, the x-axis and unit vector $\boldsymbol{i}$ point towards the Galactic Centre, the y-axis and unit vector $\boldsymbol{j}$ point in the direction of rotation, and the z-axis and unit vector $\boldsymbol{k}$ point towards the North Galactic Pole (NGP). In this frame, a star's velocity components are (V_x, V_y, V_z). Hence, we place Sgr A* at $(x, y, z) = (R_0, 0, z_0)$ kpc, where $R_0 = 8.2 \pm 0.1$ kpc and $z_0 = 25 \pm 5$ pc (Bland-Hawthorn & Gerhard 2016) consistent with the new ESO Gravity measurement (Gravity Collaboration et al. 2018), and the Sun's velocity with respect to a colocated particle on a circular orbit is $\boldsymbol{v}_{\mathbf{LSR}} = U_\odot \boldsymbol{i} + V_\odot \boldsymbol{j} + W_\odot \boldsymbol{k}$, with $(U_\odot, W_\odot) = (11.1, 7.25)\,\mathrm{km\,s^{-1}}$ (Schönrich, Binney & Dehnen 2010).

We employ Galactocentric cylindrical coordinates (R, ϕ, z) centred on Sgr A* with ϕ increasing clockwise when viewed from the north and the Sun located at $\phi_0 = \pi$. To convert velocities from the heliocentric to the Galactocentric frame, we take the angular velocity of the Sun to be $\Omega_\odot = (\Theta_0 + V_\odot)/R_0 = 30.24\,\mathrm{km\,s^{-1}\,kpc^{-1}}$ from the measure proper motion of Sgr A* (Reid & Brunthaler 2004).

2.3 Angle-action variables

Motion in the zV_z plane is simplest when cast in terms of angle-action coordinates (Binney & Tremaine 2008; Binney & Schönrich 2018). The actions J_R and J_z quantify the amplitudes of a star's oscillation parallel and perpendicular to the Galactic plane, respectively. In an axisymmetric potential, the third action J_ϕ is the component of angular momentum around the symmetry axis: $J_\phi \equiv L_z$. Each action J_i is associated with an angle variable θ_i such that $(\boldsymbol{\theta}, \boldsymbol{J})$ forms a complete set of canonical coordinates for phase space. In the potential for which they are defined, the actions are constants of motion, while the angle variables increase linearly in time $\theta_i(t) = \theta_i(0) + \Omega_i t$, where the Ω_i are the star's three fundamental frequencies. We use the software package AGAMA (Vasiliev 2018) to compute angles and actions for motion in the Galactic potential derived by Piffl et al. (2014). Our actions were compared to those computed from `galpy` (Bovy 2015) and the results are broadly similar given the observational uncertainties. The Piffl et al. (2014) potential is preferred because it is constrained to fit the well established, vertical density profile through the Sun's position (Gilmore & Reid 1983), which is necessary for deriving an accurate oscillation period for a star away from the plane. We quote actions with dimensions L^2T^{-1} as multiples of $R_0\Theta_0 = 1952\,\mathrm{kpc\,km\,s^{-1}}$ for which $\Theta_0 = 238\,\mathrm{km\,s^{-1}}$. We recognize that the actions are not true invariants over the lifetime of the Galaxy, but they are demonstrated to be useful in the halo or the disc over many orbits (e.g. Solway, Sellwood & Schönrich 2012).

3 DISC DISSECTION WITH GALAH DATA

The GALAH survey exploits the HERMES at the AAT (Sheinis et al. 2015). This instrument employs the Two Degree Field (2dF) fibre positioner at the *f*/3.3 Prime Focus to provide multiobject ($n \approx 400$), high-resolution ($\mathcal{R} \approx 28\,000$) spectra of many stars in a single shot. HERMES is a fibre-fed, multichannel spectrograph optimized to carry out Galactic archaeology from a 4-m class telescope (De Silva et al. 2015). HERMES has four optical spectrographs covering 471–490, 564–587, 647–673, and 758–788 nm for determining elemental abundances for up to 30 elements (up to 45 elements for the brightest stars). HERMES exploits a photonic comb to internally calibrate the fibre-to-fibre response across the full field of all four detectors (Bland-Hawthorn et al. 2017; Kos et al. 2018b).

Here, we use the internal data release of 505 571 stars provided to the GALAH team which includes GALAH DR2 (Buder et al. 2018) augmented with HERMES data from parallel observations of open clusters, and K2 (Wittenmyer et al. 2018) and TESS fields (Sharma et al. 2018). These new observations, which provide improved calibrations of stellar masses and gravities, were reduced with the same pipeline as DR2 (Kos et al. 2017). The additional numbers of stars are 2 498, 97 133, and 42 764, respectively. From this sample, we select stars with the *Gaia* DR2 relative parallax uncertainty of less than 20 per cent and distance $|R - R_0| < 1.0$ kpc and $|\phi - \phi_0| < 15^\circ$. These criteria yield a sample of 192 972 stars.

3.1 Chemodynamic correlations

Fig. 2 shows the density of GALAH stars in the plane of [Fe/H] versus V_z where the Sun lies at the density peak around (0,0). As [Fe/H] becomes negative, the density decreases at first gradually and then at [Fe/H] ~ -0.7 very steeply as the α-rich disc gives way to the halo. At positive [Fe/H], the fall-off in density becomes steep at [Fe/H] ~ 0.4, significantly more metal-rich than the metallicity of the local interstellar medium (ISM) determined from the small abundance dispersion of local B stars (Nieva & Przybilla 2012). This is a signature of radial migration (Sellwood & Binney 2002;

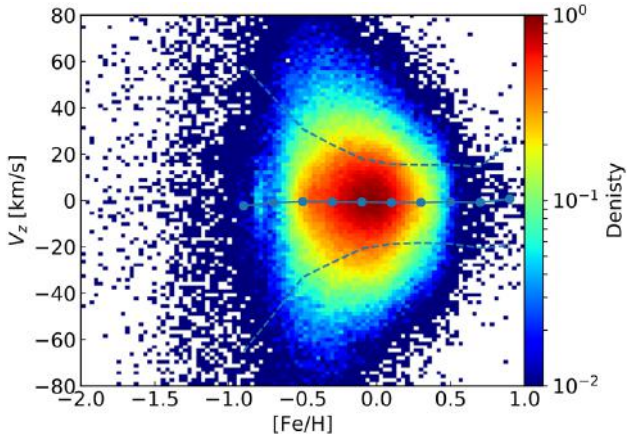

Figure 2. Normalized density of GALAH stars in the plane [Fe/H] versus V_z. This is mostly understood in terms of the well-known age–metallicity and age–velocity dispersion relations (e.g. Sharma et al. 2014). [Fe/H] is taken from the GALAH survey; V_z is determined from *Gaia* proper motions and GALAH radial velocities. The mean trend is indicated; the 1σ error tracks show the progression from the thin disc to the thick disc and halo as [Fe/H] declines.

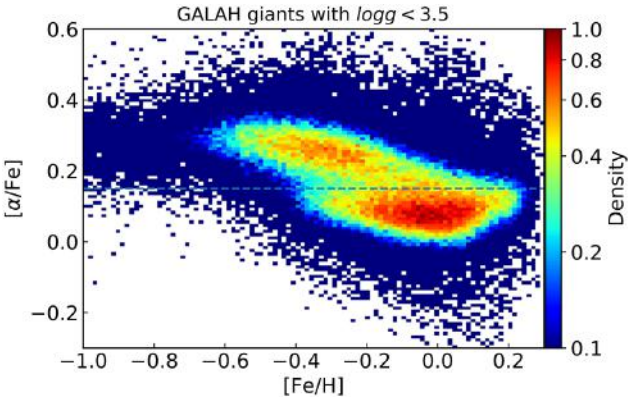

Figure 3. Normalized density of giants in the [Fe/H] versus [α/Fe] plane using data from the GALAH survey ($\log g < 3.5$). A clear separation of the high and low [α/Fe] populations is visible. The dashed boundary line distinguishes the high and low [α/Fe] populations (cf. Adibekyan et al. 2012). The simple choice of boundary is indicated in Section 4.3 where we show that the dynamical properties (actions) of the high and low [α/Fe] populations are distinct.

Schönrich & Binney 2009) that favours stars with low vertical dispersion σ_z on near circular orbits (Minchev & Famaey 2010; Daniel & Wyse 2018). We provide more evidence of disc migration in Section 4.5.

The dashed lines in Fig. 2 illustrate one standard deviation in V_z at a given [Fe/H]. This is remarkably flat at $\sim$20 km s^{-1} for [Fe/H] > -0.1, but as [Fe/H] falls below -1, it increases with ever-increasing rapidity. The increase of σ_z as [Fe/H] decreases arises from two effects: (i) the stochastic acceleration of stars causes older, more metal-poor, populations within the thin disc to have larger velocity dispersions (Aumer, Binney & Schönrich 2016), and (ii) as [Fe/H] declines, the α-rich disc is more dominant and its stars have larger σ_z (hence its thickness).

Fig. 3 shows the distribution in the ([Fe/H], [α/Fe]) plane of GALAH stars that are classified as giants ($\log g < 3.5$). The distribution is strongly bimodal. We use the horizontal dashed line to classify stars as members of either the α-rich or α-poor disc. This is a simpler definition than one used in many other studies, which divide the discs by a line that runs down toward [α/Fe] ~ 0 at the largest values of [Fe/H]. We adopt the horizontal line in Fig. 3 because it reflects the bimodality that is unambiguously present here and because GALAH captures significantly fewer α-rich stars than α-poor ones, so it is better to contaminate the α-poor sample with a few α-rich stars than allow significant contamination of the α-rich sample by outliers from the α-poor disc. A more complicated selection, such as those employed by Bensby et al. (2014) and Hayden et al. (2015), has the potential to contaminate the sample with stars that have more thin disc kinematics. Specifically, Haywood et al. (2013) and Hayden et al. (2017) show that the metal-rich intermediate α stars have kinematics similar to the thin disc.

Fig. 4 contrasts the action distributions of stars of different chemical compositions. From top to bottom, the panels of the left-hand column (a), (d), and (g) show the distributions over J_R, J_z, and L_z for all stars. The middle and right-hand columns separate them into α-rich and α-poor stars, respectively. For a star describing a perfect circular orbit confined to the Galactic plane at the Sun's radius, $L_z = J_\phi = 1$, $J_R = 0$, and $J_z = 0$. For metallicities below [Fe/H] ≈ -1, the transition to the high-energy, low-density stellar halo (low L_z) in all panels is clear. Panel (h) reveals that, in the α-rich disc, L_z tends to grow with increasing [Fe/H], while panel (i) shows that the opposite correlation prevails in the α-poor disc. The decrease of [Fe/H] with increasing L_z in the α-poor disc reflects the radial metallicity gradient (i.e. metal-poor stars are from the outer disc and have large L_z) that is a general feature of galaxies discussed by many authors (Chiappini, Matteucci & Romano 2001).

The α-rich disc shows the *opposite* correlation, a remarkably clear trend discovered by Spagna et al. (2010) that is poorly understood. Schönrich & McMillan (2017) argue that the effect arises because the α-rich disc grew rapidly in radial extent on a $\sim$Gyr time-scale coincident with the transition from Type II to Type Ia supernova enrichment. In contrast, the accreting proto-cloud that formed the thick disc may have undergone a rapid collapse over roughly the same time-scale, with stars forming during the collapse phase (outside–in scenario).

We can relate the action-metallicity dependencies to the better known metallicity–dispersion relations in the following way. For all actions, we may write

$$2\pi J_i = \oint \dot{x}_i \, \mathrm{d}x_i = \frac{1}{\Omega_i} \int_0^{2\pi} (\dot{x})^2 \, \mathrm{d}\theta_i = \frac{2\pi}{\Omega_i} \langle v_i^2 \rangle. \quad (1)$$

Thus the time average of a star's squared velocity component is related to the action J_i through the associated frequency Ω_i such that $\langle v_i^2 \rangle = \Omega_i J_i$. Passing from this result for time averages for individual stars to population averages over the stars that reach a given place is non-trivial, but it generally follows that

$$\sigma_i^2 / \sigma_j^2 = \langle \Omega_i J_i \rangle / \langle \Omega_j J_j \rangle \quad (2)$$

where $\langle . \rangle$ is an appropriate average. When dividing the median tracks in Figs 4(b) and (e) for the α-rich disc, we find that $\langle J_z / J_R \rangle \approx 0.1$ near solar metallicity, asymptoting to 0.25 in the metal-poor limit. In the α-poor disc, the same trend is seen but the asymptotic limit is significantly lower at 0.2. More broadly, we may write

$$\sigma_z / \sigma_R \approx \sqrt{\langle \Omega_z / \Omega_R \rangle} \sqrt{\langle J_z / J_R \rangle}. \quad (3)$$

In Fig. 5, we note that $\langle \Omega_R / \Omega_z \rangle \approx 0.6 \pm 0.1$ such that $\sigma_z / \sigma_R \approx 0.6 \pm 0.1$ consistent with both the Gaia-ESO survey ($\sigma_z / \sigma_R \approx 0.7$;

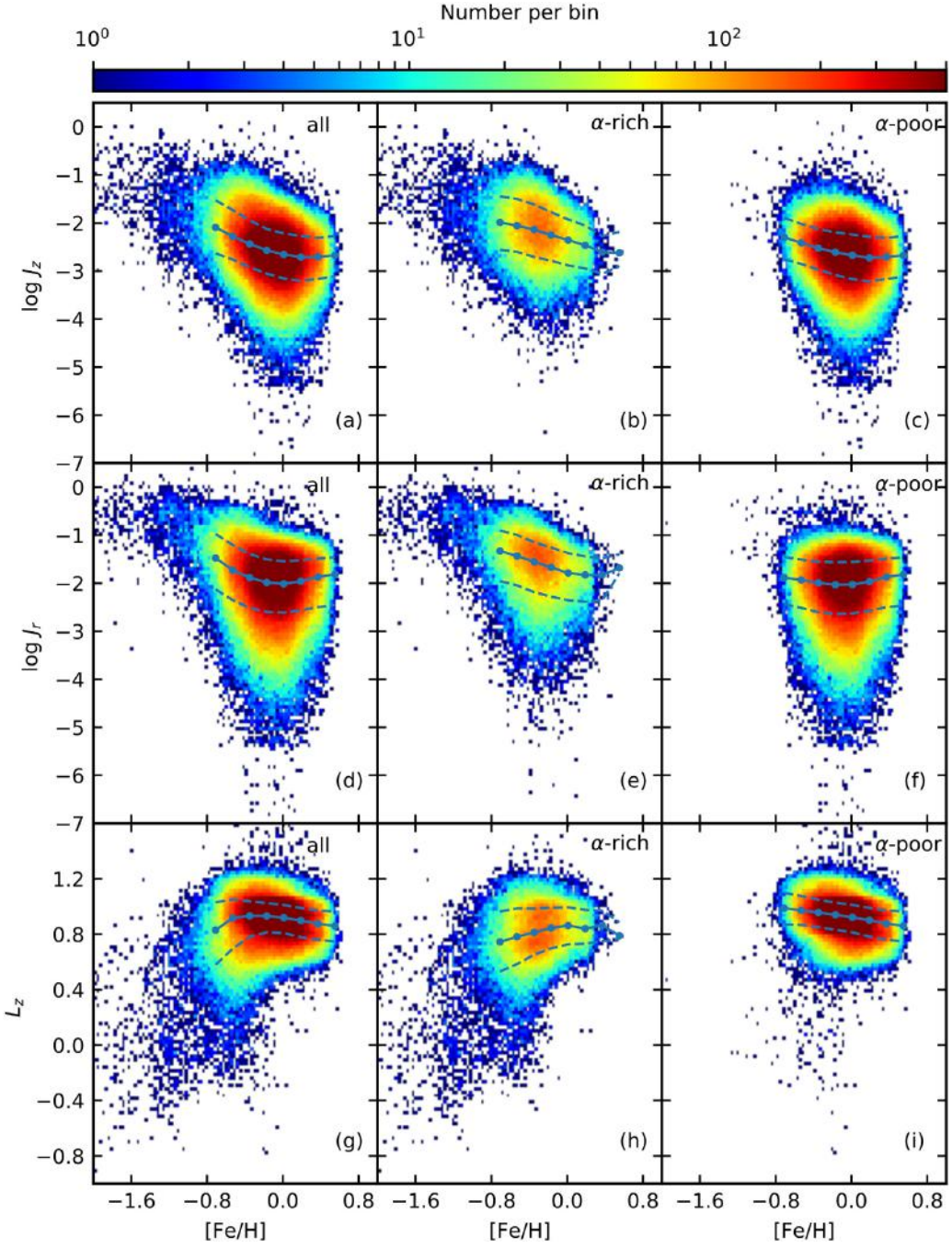

Figure 4. Stellar metallicity versus actions for stars that lie within 1 kpc of the Sun in both GALAH and *Gaia* DR2 (Fig. 1); the normalized stellar densities are shown in colour. The actions are computed with the AGAMA code using the Pifffl et al. (2014) galactic potential, with the normalization defined in Section 2. The left-hand column includes all stars, the middle column is for the α-rich disc, and the right-hand column for the α-poor disc. (a)–(c) [Fe/H] versus $\log J_z$, (d)–(f) [Fe/H] versus $\log J_R$, and (g)–(i) [Fe/H] versus $J_\phi \equiv L_z$. The mean trend and 1σ dispersion tracks are also shown.

Guiglion et al. 2015)[3] and the RAVE survey ($\sigma_z/\sigma_R \approx 0.6$; Binney et al. 2014).

In Fig. 4(f), the J_R distribution of the α-poor stars has a much sharper top-right corner than the corresponding distribution of J_z shown in panel (c). This indicates that the most metal-rich stars extend to the largest values of J_R but they shun the largest values of J_z. This phenomenon has two possible explanations. One is that spiral structure almost instantaneously accelerates stars to significant random velocities within the plane but it takes significant time for molecular clouds to convert in-plane motion to vertical motion (Aumer et al. 2016). The other possible explanation is that the most metal-rich stars can enter the GALAH sample only by migrating outwards from their birth radii, and stars with large J_z are

[3]There is a typographical error in Guiglion et al. (2015) stating that $\sigma_R/\sigma_z \approx 0.7$ in conflict with the data presented in their fig. 11; their quoted Binney et al. (2014) result is also misstated.

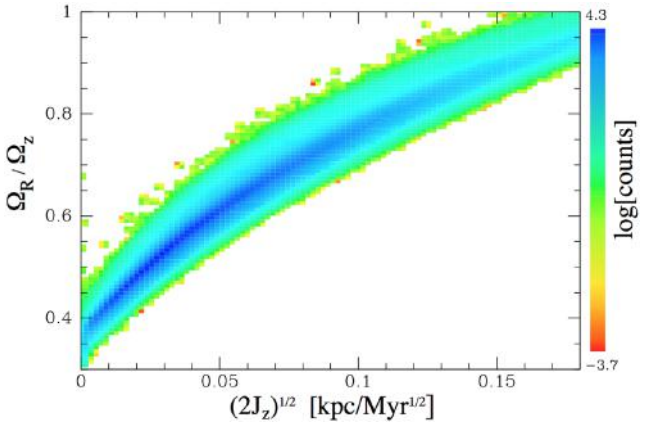

Figure 5. The frequency ratio Ω_R/Ω_z versus $\sqrt{2J_z}$ for orbits calculated in a realistic Galactic potential; the ratio for most stars lies in the range 0.5–0.7. The factor 2 in front of J_z ensures that the area inside a curve of constant J_z is $2\pi J_z$ in the zV_z plane. Note that a range of frequencies operates in R and z for all values of J_z.

less likely to migrate than stars with small J_z (Solway et al. 2012). It is interesting to note that the upper envelopes of the J_R and J_z distributions of the α-rich stars are almost identical with the most metal-rich stars shunning the highest values of both actions. We discuss the expected signatures of stellar migration in more detail in Section 4.5.

In an upcoming paper, Hayden et al. (2019) derive new velocity dispersion–metallicity relations from the GALAH survey. They take stars (mostly dwarfs) within 500 pc of the Sun and measure the velocity dispersion profiles in all three components (V_R, V_ϕ, V_z) for populations based on their metallicity and [α/Fe] abundance. The velocity dispersions increase smoothly as [α/Fe] increases for a fixed metallicity, [Fe/H]. The velocity dispersions also increase as metallicity decreases for stars at a fixed [α/Fe]. These results mirror those presented here for the actions, with the kinematics of the α-rich population becoming more like the α-poor population as [Fe/H] declines. The most metal-poor, α-poor stars have larger velocity dispersions than those with higher metallicities. These stars are the scatter of blue points in Figs 4(c), (f), and (i) that fall outside the main trends and make up the outer flaring disc.

4 THE PHASE SPIRAL

Antoja et al. (2018) selected stars from *Gaia* DR2 that lie in the thin cylinder $|R - R_0| < 0.1$ kpc with $|\phi - \phi_0| < 7.5°$. To revisit the phase spiral in more detail, we expand the volume by an order of magnitude to $|R - R_0| < 1.0$ kpc and $|\phi - \phi_0| < 15°$. This expansion ensures that a useful number of GALAH stars are included. As in Antoja et al. (2018), we restrict consideration to stars that satisfy $\sigma_\varpi/\varpi < 0.2$ so that distances can be readily inferred from parallaxes (Schönrich & Dehnen 2018). The domain of our study and that of Antoja et al. (2018) is shown in Fig. 1.

Following Antoja et al. (2018), the top left panel of Fig. 6 plots the mean value of V_ϕ in the zV_z plane. The overall tendency is for the centre of the panel to be red, signalling large values of $\langle V_\phi \rangle$, while the edges are blue because there $\langle V_\phi \rangle$ is lower. This low-order structure reflects the familiar phenomenon of asymmetric drift: stars that make large vertical excursions (large $|z|$ and/or large $|V_z|$) tend to have guiding centres inside R_0 and are consequently visiting us near apocentre. Superposed on the low-order trends in Fig. 6 is a prominent one-armed spiral of stars with anomalously high $\langle V_\phi \rangle$.

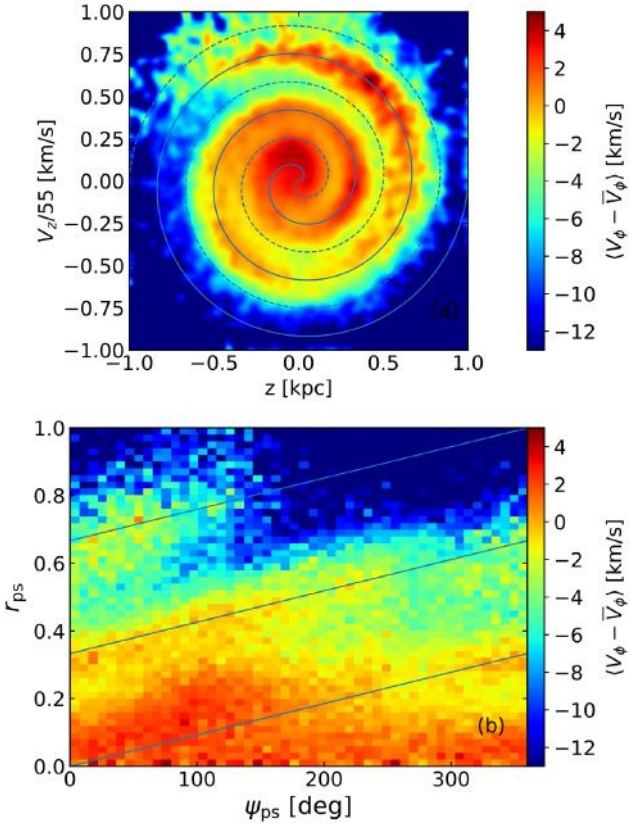

Figure 6. Kinematic properties of stars in the solar neighbourhood using data from *Gaia* DR2. Stars were selected to be within $|R - R_0| < 1.0$ kpc and $|\phi - \phi_0| < 15°$. Top: map of $\langle V_\phi(z, V_z) - \overline{V}_\phi \rangle$ with the volume-weighted median value ($\overline{V}_\phi = 228.3$ km s^{-1}) subtracted. The archimedean spirals are defined in equation (3). Bottom: the unwound spiral pattern as a function of r_{ps} (dimensionless) and ψ_{ps} (in degrees). The three diagonal lines wrap around every 2π and thus correspond to three different r_{ps} intervals in the zV_z plane. Note the underlying velocity gradient in r_{ps} due to the asymmetric drift.

The benefits of expanding the sample volume are clear, but there is also a penalty. The phase spiral in Fig. 6 shows the change of $\langle V_\phi \rangle$ with position in the zV_z plane. Comparing the stellar kinematics in the red and yellow parts of the spiral, the change of $\langle V_\phi \rangle$ is due to a shift in the shape of the distribution of V_ϕ, but only for stars within $\approx$25 km s^{-1} of the peak in the $\langle V_\phi \rangle$ distribution. Stars further from the peak are not affected: they have the same distribution in the red and yellow parts of the spiral. $\langle V_\phi \rangle$ is a proxy for the guiding centre radius, so the shift in $\langle V_\phi \rangle$ is just a shift in the mean guiding centre radius between stars in the red and yellow parts of the phase spiral. This shift corresponds to only 5 km s^{-1} in $\langle V_\phi \rangle$ or roughly 200 pc in guiding centre radius. By increasing the radial interval from 200 pc to 2 kpc, the small shift in the mean guiding centre radius will be masked by including a much larger overall range of guiding centre radii. On the other hand, the shot noise is reduced.

In Fig. 6, a solid black line has been drawn roughly along the crest of this spiral as follows. A system (r_{ps}, ψ_{ps}) of polar coordinates are defined for the zV_z plane by

$$r_{ps} = \sqrt{(V_z/55\,\mathrm{km\,s^{-1}})^2 + (z/\mathrm{kpc})^2}$$
$$\psi_{ps} = \tan^{-1}[(V_z/55\,\mathrm{km\,s^{-1}})(z/\mathrm{kpc})^{-1}] \quad (4)$$

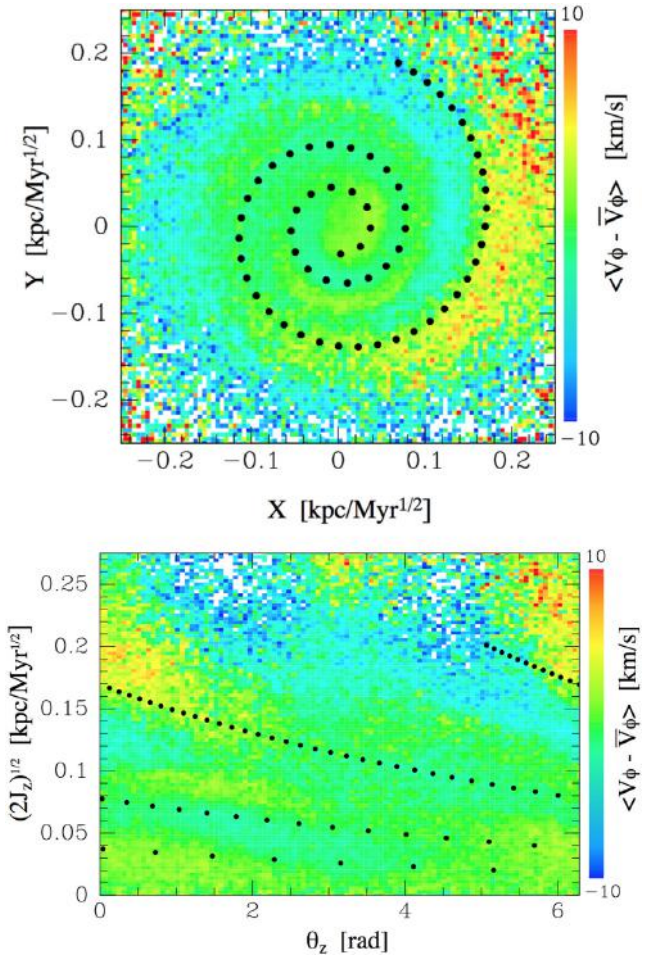

Figure 7. Top: the spiral in the angle-action coordinates defined by equation (6). The colour scale shows $\langle V_\phi(z, V_z) - \overline{V}_\phi \rangle$, where the overline means the average over θ_z at the given J_R. Bottom: the spiral unwrapped by plotting same quantity in the angle-action coordinates analogous to (r_{ps}, ψ_{ps}). The dots show the relation in equation (7). The action-angle figures convey the same information as the projections in Fig. 6.

where z is in units of kpc. The curve is then the Archimedean spiral

$$r_{ps} = k(\psi_{ps} + \eta) \tag{5}$$

where $k = 1/(6\pi)$ is a constant and $\eta = 0, \pi$ (solid, dashed) allows the spiral to be rotated. The right-hand panel of Fig. 6 shows how, when $\langle V_\phi \rangle$ is plotted in (r_{ps}, ψ_{ps}) space, the spiral unravels into sloping straight lines that wrap from the right to the left edge of the plot on account of the periodicity of ψ_{ps}.

Within the zV_z plane, stars move clockwise on oval curves: our adopted scaling $z/\,\mathrm{kpc} \sim V_z/55\,\mathrm{km\,s^{-1}}$ leads to circles consistent with the discovery paper (Antoja et al. 2018). The angular frequency at which a star moves on its circle decreases as the circle's radius increases, so an initially radially directed line of stars is steadily sheared into a spiral like that evident in Fig. 6.

Using angle-action coordinates, we can quantify this phase-wrapping process. Fig. 7 shows the plane defined by coordinates

$$X \equiv \sqrt{2J_z}\,\cos\theta_z \qquad Y \equiv -\sqrt{2J_z}\,\sin\theta_z\,, \tag{6}$$

where the minus sign is included in the definition of Y so stars circulate clockwise as θ_z increases.[4] If the stellar z oscillations were harmonic, these coordinates would be simply linearly scaled versions of z and V_z. In reality, they have a complex relation to (z, V_z) because the z oscillations are strongly anharmonic. In the XY plane, stars move exactly on circles of radius $\sqrt{2J_z}$ at the angular velocity Ω_z that can be computed as a function of the radius. The dots in Fig. 7 trace the curve

$$\theta_z = \Omega_z(J_{\phi 0}, J_z)\,t_o + 0.75 \tag{7}$$

where $J_{\phi 0}$ is the angular momentum of a circular orbit at R_0 and $t_o = 515$ Myr. This curve delineates quite well the inside of the blue spiral. The colour scale in this figure shows the amount by which $\langle V_\phi \rangle$ deviates from its average value around the relevant circle. The spiral, which decreases in amplitude towards the centre, can now be traced all the way to the centre.

Binney & Schönrich (2018) argue that the spiral arises because, at a given value of J_z, the values of Ω_z vary systematically with L_z: stars with smaller guiding-centre radii have higher frequencies. Hence, when some event bunches stars in θ_z, the stars with smaller values of L_z move ahead of the stars with larger L_z as they move around their common circle in the xy plane. The dots in Fig. 7 mark the locations reached by stars that lie at the centre of the L_z distribution, so the part of each circle on which V_ϕ is below average should lie at later times on the clock than the part at which V_ϕ is above average. This is precisely what we see in the upper panel of the figure.

4.1 Slicing by location

Fig. 8 explores how the properties of the phase spiral vary with location and volume in the Galaxy. Panel (a) exploits the data used by Antoja et al. (2018) that are confined to a narrow vertical cylinder local to the Sun. Panel (b) is the expanded sample around the Sun studied in Fig. 6. The volume of the latter sample is 20 times larger than the former, yet the spiral pattern remains essentially the same. The remaining panels, which also use larger volumes, examine samples in neighbouring spheres close to the solar neighbourhood, two offset to larger and smaller radii (c) and (d), and two offset in both directions in azimuth (e) and (f).

As illustrated in Fig. 1, panel (c) examines a sample centred at $R = R_0 - 0.5$ kpc, while panel (d) explores a sample centred at $R = R_0 + 0.5$ kpc. The spiral pattern is evident but shows clear differences from inner to outer disc, with the outer disc spiral being stronger at higher $|z|$. The inner part of the spiral in (c) is stretched vertically relative to (d) consistent with the stronger disc gravity (see below).

Panel (e) explores a sample with Galactocentric longitude $|\phi - (\phi_0 + 7.5^\circ)| < 7.5^\circ$, while panel (f) explores a sample with $|\phi - (\phi_0 - 7.5^\circ)| < 7.5^\circ$. There is little evolution with azimuth over the inner spiral; the outer spiral varies with azimuth in addition to radius. The outer part of the phase spiral being more prominent at larger Galactocentric radius and smaller azimuthal angle has an important consequence that we return to below.

We also inspected the 2-kpc diameter volume centred at $R = R_0 \pm 1$ kpc; the phase spiral was evident but less well defined due to the smaller number of stars and the larger cumulative errors on measured parameters.

[4]The factor 2 in equation (6) ensures that the area inside a curve of constant J_z is $2\pi J_z$, as it is in the zV_z plane.

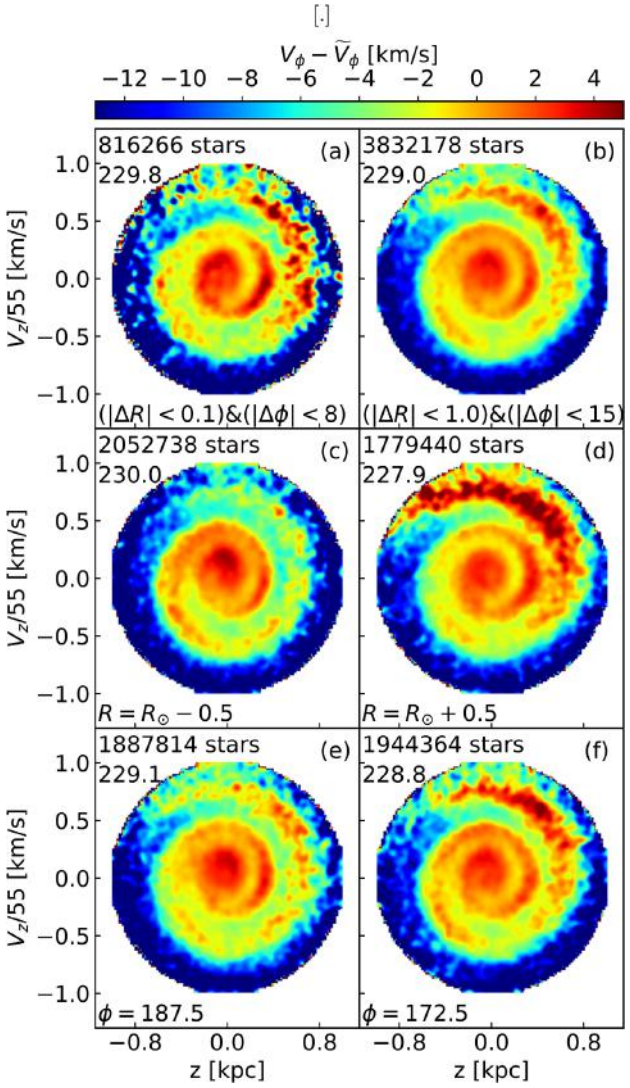

Figure 8. Kinematic properties of stars in the solar neighbourhood in the zV_z plane using data from *Gaia* DR2 explored by volume and location. The colour code shows the deviation in volume-weighted V_ϕ with respect to the median value quoted in each panel along with the number of stars used. (a) Stars with $|R - R_0| < 0.1$ kpc and $|\phi - \phi_0| < 7.5^\circ$ presented in Antoja's original analysis for a narrow vertical cylinder. (b) Stars with $|R - R_0| < 1.0$ kpc and $|\phi - \phi_0| < 15^\circ$ highlighting the same phase spiral over the 20× larger GALAH volume. (c) Stars with $(|R - (R_0 - 0.5)| < 1.0$ kpc and $|\phi - \phi_0| < 15^\circ$. (d) Stars with $|R - (R_0 + 0.5)| < 1.0$ kpc and $|\phi - \phi_0| < 15^\circ$. Note the inner spiral in (c) is vertically elongated consistent with the smaller Galactic radius; the outer spiral in (d) is more prominent at larger radius. (e) Stars with $|R - R_0| < 1.0$ kpc and $|\phi - (\phi_0 + 7.5^\circ)| < 7.5^\circ$. (f) Stars with $|R - R_0| < 1.0$ kpc and $|\phi - (\phi_0 - 7.5^\circ)| < 7.5^\circ$. The form of the spiral is remarkably invariant across most panels, but different sections can be enhanced relative to others, e.g. note the asymmetry in azimuth and radius in the prominence of the outer spiral (d and f compared to c and e). (ϕ is quoted in degrees).

4.2 Slicing by chemistry

In Fig. 9, we show how the distribution of stars in the zV_z plane varies with metallicity. As a result of GALAH's selection criterion ($|b| > 10^\circ$), there is a deficit of stars at small z. On account of the age–metallicity relation, metal-rich stars tend to be younger than metal-poor ones, so by the age–velocity dispersion relation they

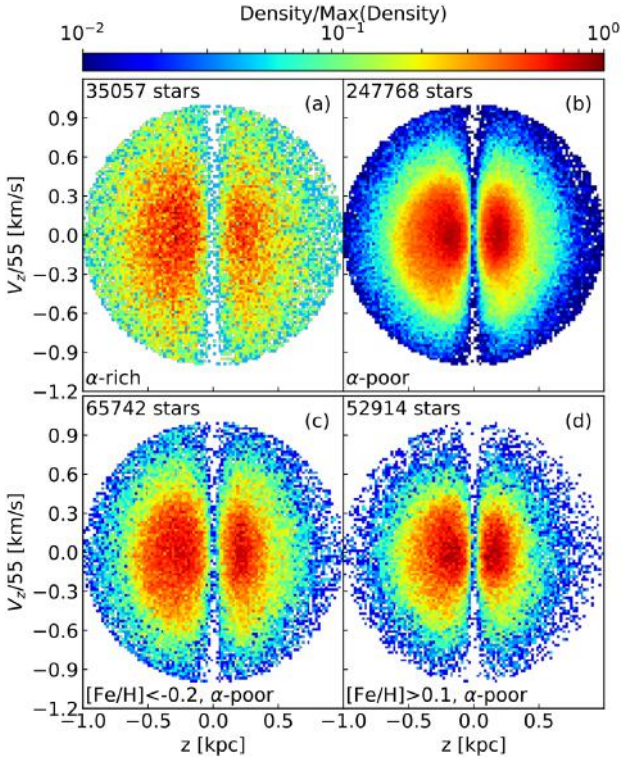

Figure 9. The density of GALAH stars in the zV_z plane as a function of chemistry: (a) α-rich disc, (b) α-poor disc, (c) α-poor, metal-poor disc, and (d) α-poor, metal-rich disc. The number of stars used in each panel is indicated.

are more strongly concentrated to the centre of the zV_z plane than metal-poor stars, and especially more than α-rich stars, which, as discussed in Section 3.1, reach exceptionally large values of J_z.

As Fig. 10 shows, these differences by chemical composition in the locations of stars within the zV_z plane impact the visibility of the phase spiral in different chemically defined populations. Panel (a) shows the phase plane for α-rich stars in the sense of Fig. 3, while panel (b) shows the α-poor stars (cf. Adibekyan et al. 2012). Additionally, we subdivide the α-poor disc into (c) metal-poor ([Fe/H]<−0.2) and (d) metal-rich ([Fe/H]>0.1) bins. The phase spiral shows a clear trend in metallicity across the zV_z plane: for metal-rich stars, the inner spiral is strong; and for metal-poor stars, particularly in the α-poor disc, the outer spiral is strong.

The α-rich disc (a) shows much weaker evidence for the phase spiral than the α-poor disc (b), but in part this may reflect the order of magnitude smaller size of the sample. To check if this fully accounts for the difference, we examined samples of α-poor stars that were restricted to 31 666 stars by random subsampling: even these attenuated samples of α-poor stars showed the spiral more clearly than the α-rich sample. This indicates that the spiral pattern in the α-rich disc is intrinsically weaker than in the colder α-poor disc.

As we vary the metallicity of the α-poor stars under study, two effects are in play. First, on account of the disc's radial metallicity gradient, the mean guiding-centre radius of the sample will decrease as the metallicity is increased, and we saw above (Fig. 8) that decreasing the radius weakens the outer spiral. Secondly, by the age–velocity dispersion relation, the zV_z footprint of the stars will move inwards as metallicity increases (Fig. 9), which will again weaken the spiral (Fig. 7). In line with these expectations, in Fig. 10, the

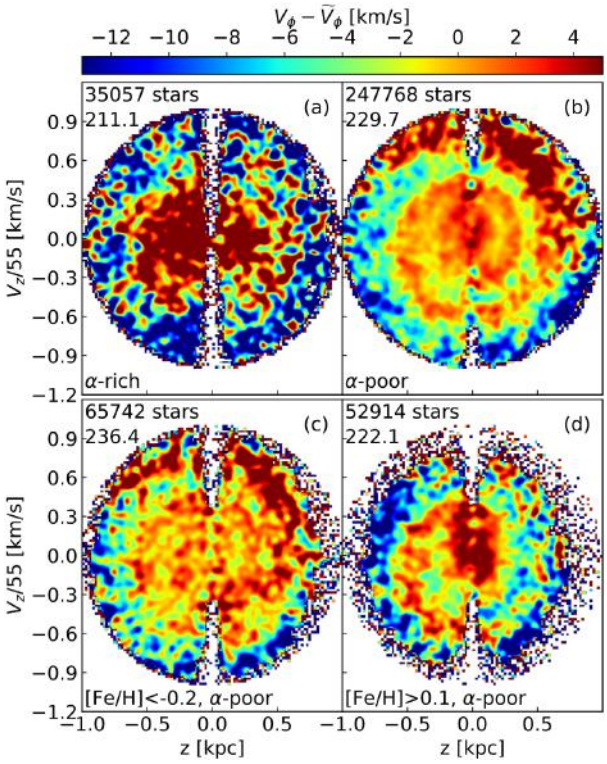

Figure 10. Analogue of Fig. 9 but showing $\langle V_\phi \rangle$ instead of the density of stars in the zV_z plane. In panel (d), the inner phase spiral is prominent in the younger, α-poor, metal-rich disc, but is not obviously evident in the older stars, i.e. (a) and (c) the α-rich disc and the α-poor, metal-poor disc. (b) and (d) The outer spiral is most prominent in the α-poor, metal-poor disc (b,c).

outer spiral is clearest for the most metal-poor stars (c) and becomes weaker as we increase the metallicity of the sample (d).

The trend in the spiral pattern with metallicity is smoothly varying with no evidence for a chemically homogeneous or single-age population (e.g. star cluster) dominating the phase spiral at fixed V_ϕ. This rules out the idea that it is associated with one or more large disrupting star clusters.

4.3 Slicing by actions

In Fig. 11, we explore how the zV_z phase plane varies when stars are selected by the values of their actions J_R and L_z. Stars are split by whether their radial action is greater than (left-hand panels: a, c, and e) or less than (right-hand panels: b, d, and f) the median value over the *Gaia* volume, $\overline{J}_R = 0.01$. Stars with larger J_R move on more eccentric orbits. Near the centre of the phase plane, the spiral is much more clearly traced by stars with less eccentric orbits. In fact, panels (b) and (f) provide the clearest manifestation to date that the phase spiral can be traced to the origin of the vertical phase plane. Notice that the V_ϕ scales of the two panels are quite different, so V_ϕ for the low-eccentricity stars is systematically larger than for the high-eccentricity stars. This indicates that stars with large J_R typically have guiding-centre radii inside R_0, a consequence of both the steep radial density gradient within the disc and the outward decline in σ_R.

The lower row in Fig. 11 shows the effect of further splitting stars by their values of $L_z \equiv J_\phi$. The guiding centres of stars with $L_z > 1$ lie outside R_0, and conversely for stars with $L_z < 1$. Comparison of panels (d) and (f) shows significant difference in the structure of the

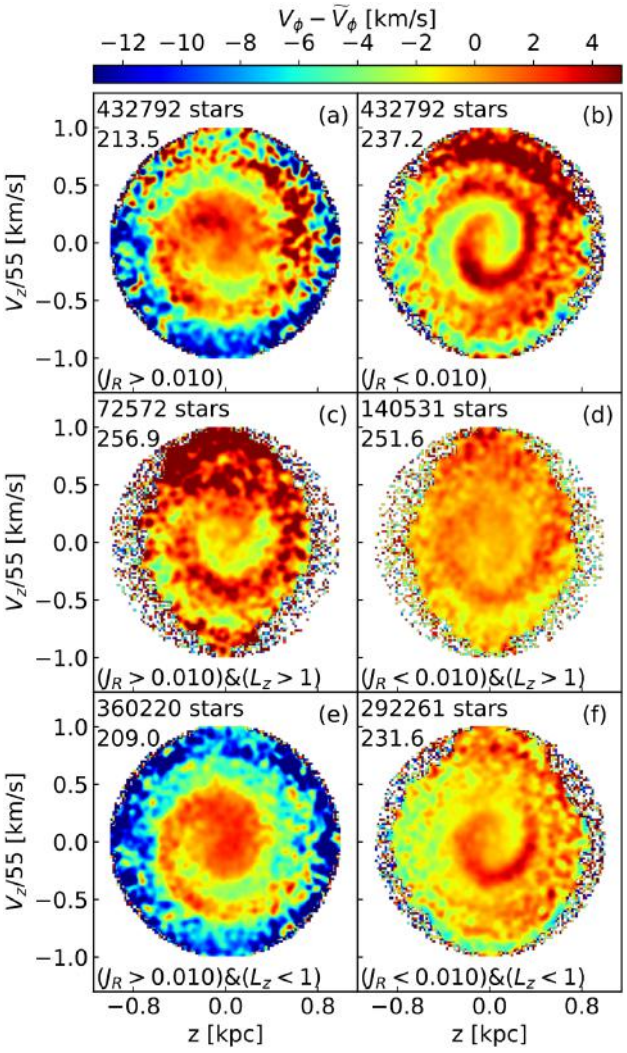

Figure 11. Dissection by actions (J_R, $J_\phi \equiv L_z$) over the original Antoja volume ($|\Delta R| < 0.1$ kpc). The left-hand panels show stars with $J_R > \overline{J}_R$, where $\overline{J}_R$ is the median value over the volume. The right-hand panels show stars with $J_R < \overline{J}_R$. The character of the phase spiral is very different for stars with eccentric (a) compared to more circular (b) orbits. Thus, we divide the distribution in action further: (c) $J_R > \overline{J}_R$, $L_z > 1$; (d) $J_R < \overline{J}_R$, $L_z > 1$; (e) $J_R > \overline{J}_R$, $L_z < 1$; and (f) $J_R < \overline{J}_R$, $L_z < 1$. Stars with $L_z > 1$ have guiding-centre radii outside the Solar Circle. Comparison of panels (f) and (d) reveals that the tight inner spiral arises from stars with less eccentric orbits and guiding radii inside R_0 that reach apogalacticon in the solar neighbourhood. Comparison of panels (c) and (e) shows that stars on eccentric orbits from the outer disc are much less relaxed.

innermost portion of the phase spiral – stars with smaller L_z form a tighter spiral that reaches the centre sooner. Panel (c) shows that the stars on eccentric orbits with large guiding centres are very far from relaxed, with a strong bias towards values of $\psi_{ps} \sim 90°$.

4.4 Slicing by ages

The *Gaia* DR2 data release provides accurate photometry in three bands that we exploit here, i.e. the super-broad-band G filter, and for the split bands G_{BP} (blue) and G_{RP} (red) (Jordi et al. 2010). We use the *Gaia* colour ($G_{BP} - G_{RP}$) to estimate crude photometric stellar ages. *Gaia* also provides a reddening estimate; we use these to demonstrate some problems but do not use them in the

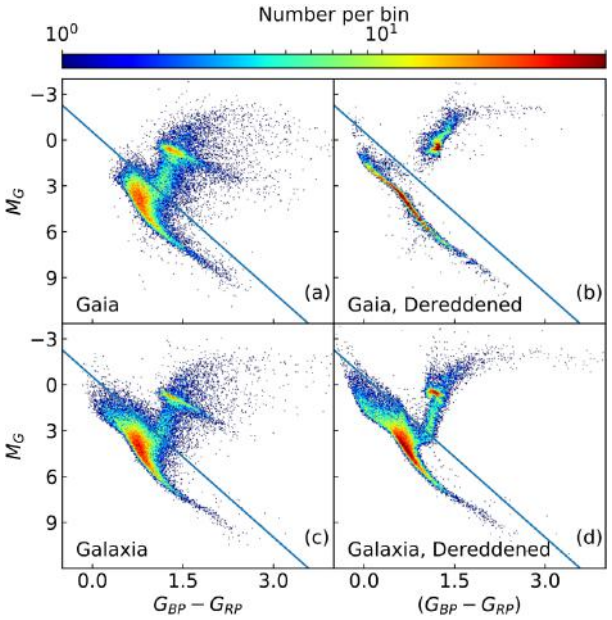

Figure 12. The colour–magnitude distribution of *Gaia* stars in the solar neighbourhood and that of a mock sample generated with the GALAXIA model for the Galaxy (Sharma et al. 2011) which includes a sophisticated treatment of the dust extinction. The *Gaia* sample is similar to that used by Antoja et al. (2018) and consists of stars with valid radial velocities, less than 20 per cent error on parallax, $|\Delta R < 1.0|$ kpc, $|\Delta\phi| < 15^\circ$, and $|\Delta z| < 1$ kpc. The mock sample was generated to match the G magnitude distribution and the selection criteria of the *Gaia* sample. Qualitatively, the raw counts in the colour–magnitude diagram uncorrected for dust extinction agree very well. The dereddened data and models agree less well because the dereddened *Gaia* stars are a biased sample; we do not use this sample in our analysis. The diagonal blue line is how we separate giants (upper) from dwarfs (lower); see the main text.

final analysis for two reasons. First, they are not available for all stars. Secondly, the velocity dispersion of the bluest stars proves larger when we use dereddened colours than the raw colour, which indicates that dereddening contaminates a 'blue' sample with older, actually redder, stars.

To calibrate the age-colour relation, we use GALAXIA to generate a mock catalogue for all stars in the GALAH volume and from them derive *Gaia* magnitudes and colours. GALAXIA uses Bayesian estimation with a scheme that takes into account the initial mass function, the star formation rate, and a sophisticated treatment for dust extinction (Sharma et al. 2011; Sharma 2017). In the left-hand panels of Fig. 12, the resulting raw distribution closely matches the *Gaia* data over the same volume. The dust-corrected photometry matches less well because the *Gaia* photometry with dust corrections represent a biased sample that is not accounted for in the GALAXIA model.

In Fig. 13, we derive from GALAXIA the centres and widths of the distributions of age at a given colour. The profiles are given for both the extinction-corrected and uncorrected colours, both of which show a monotonic increase in age with colour up to $G_{BP} - G_{RP} \approx 0.75$ (3 Gyr). Beyond here, the *Gaia* colour is a poor tracer of age. The separation of giants and dwarfs is shown in Fig. 12. We select dwarfs as $M_G < 3.5\,(G_{BP} - G_{RP} - 0.15)$, where M_G is the absolute magnitude derived using G-band photometry and the parallax-derived distance.

In Fig. 14, we show the $\langle V_\phi(z, V_z)\rangle$ map in the zV_z plane for dwarfs and giants. The dwarfs are further split up into three different age

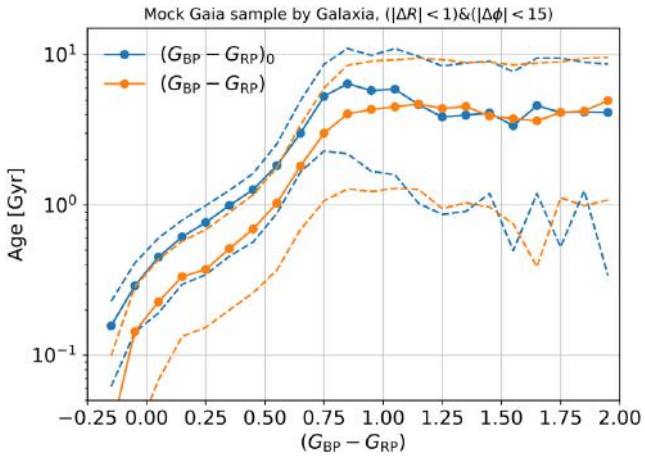

Figure 13. Given the assumed model and selection function for the Galaxy of Fig. 12, we derive a mean stellar age as a function of the *Gaia* colour for the dwarf stars. The lower solid curve is based on the raw *Gaia* photometric data uncorrected for dust extinction; the 16 and 84 percentile ranges are shown as dashed lines. The upper curves are the *Gaia* photometric data corrected for dust extinction. Age discrimination is impossible beyond about 3.5 Gyr.

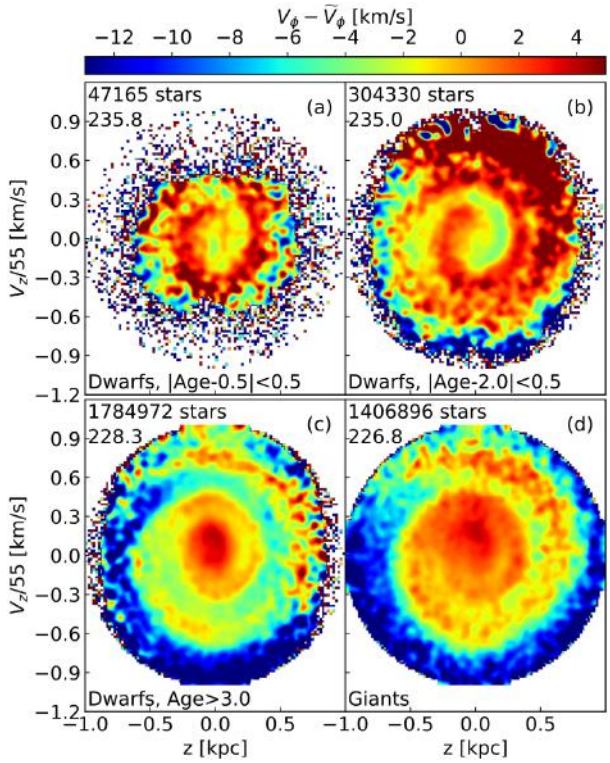

Figure 14. An analysis of the *Gaia* photometry over the GALAH volume in the zV_z plane showing crude stellar ages for (a)–(c) dwarfs and (d) giants. (a) and (b) Stars younger than about 3 Gyr emphasize the 'hook' at the centre of the phase spiral. This feature closely resembles Fig. 11(b) for which $J_R < 0.01$, i.e. younger stars from the local disc are on more circular orbits. The old dwarfs (c) and giants (d) resemble Fig. 11(a) for which $J_R > 0.01$, i.e. the older stars are on more elliptic orbits.

slices. The vertical extent increases with age due to the age–velocity dispersion relation. The giants and the oldest dwarfs have a similar distribution in age but we suspect the oldest stars are restricted in z as compared to giants because of the selection function limit ($G < 14$): red dwarfs are intrinsically fainter and harder to detect at high z.

For the dwarfs, the spiral exhibits a systematic trend with age. The inner 'hook' of the phase spiral (a and b) is stronger and clearer for stars younger than 3 Gyr; for older stars (c and d), the centre is more filled in. The 16 and 84 percentile age range for giants is about 1–9 Gyr, with a median age of 3.4 Gyr. The old dwarfs and giants (c and d) have a similar distribution in the zV_z plane although the outer phase spiral for giants (d) is more diffuse, presumably because they arise from a larger volume in (R, z). For younger dwarfs (Figs 14a and b), the inner hook closely resembles that of stars with $J_R < 0.01$ (Fig. 11b) as expected as these are stars on more circular orbits.

This raises an important question. Were the younger stars perturbed or kicked into the spiral pattern after they were born, or did they form from gas which was perturbed into the spiral pattern? If the former, this suggests that it is more difficult to excite a spiral pattern within an old, dynamically hot population. Conversely, if the latter applies, this may mean the pattern is stronger and more coherent in the gas phase. Given that collisionless stars and gas respond slightly differently to a perturbation in the potential, the two scenarios may lead to different phase distributions for the younger stars.

In a forthcoming paper, we test these ideas using an N-body simulation that has a disc continuously forming stars while interacting with the Sgr dwarf. Future HI surveys should look for the kinematic signatures of corrugation waves in the local disc. With sufficient information on transverse motions, clumpy gas could even exhibit some of the characteristics of the phase spiral. We return to this point in Section 8.2.

4.5 Stellar migration

In Section 3.1, we presented preliminary evidence for stellar migration based on metal-rich stars in the α-poor disc being limited to small values in V_z and J_z. The important point here is that stellar migration, as distinct from other scattering processes, is only efficient for stars close to the plane where the spiral arm resonances operate (Sellwood & Binney 2002). The newly furnished analysis in this section provides an even stronger case because efficient stellar migration heavily favours stars on circular orbits, which we also observe for the same stars.

In an important study, Nieva & Przybilla (2012) examine the elemental abundances of the local B star population and diffuse ISM. These stars reflect the local gas-phase abundances in the recent past ($\lesssim$50 Myr). They establish a high level of chemical homogeneity across the young population, in agreement with the gas phase (Sofia & Meyer 2001). The authors demonstrate that the Sun is too metal-rich for our neighbourhood and must have migrated from its birthplace near[5] $R \sim 5$ kpc.

In Figs 10(c) and (d), we compare metal-rich and metal-poor stars in the zV_z plane specifically for the α-poor stars. The inner part of the phase spiral is dominated by the metal-rich stars ([Fe/H] > 0.1). In Figs 11(f) and 14(a) and (b), we see a remarkable correlation. The innermost spiral is seen most clearly in dwarfs younger than 3 Gyr, and these stars are on near circular orbits consistent with their age. Their guiding radii lie inside of the Solar Circle. Thus, the metal-rich stars in GALAH must also have migrated outwards from the inner disc where they were formed over the past few billion years. Consistent with that picture, most migration models (Roškar et al. 2012; Vera-Ciro et al. 2014; Daniel & Wyse 2018; Minchev et al. 2018) find that stars on circular orbits and close to the plane are those that move most easily, and this is what we see (cf. Solway et al. 2012).

It is therefore interesting to consider the origin of metal-rich stars that are *not* on circular orbits in the solar neighbourhood. Such stars are observed to exist in the GALAH sample within both the α-rich and α-poor discs (Fig. 4). These stars appear to be older than the circularized population and conceivably require another transport process (see Section 3.1), or a more nuanced understanding of the Sellwood & Binney (2002) proposal.

A star in a near-circular orbit is captured in a spiral-arm corotation resonance (Daniel & Wyse 2015) and moves back and forward along the Jacobi integral line $E_J = E - \Omega \cdot L_z$ tangent to the circular orbit curve in the (E, L_z) plane (see fig. 1 in Sellwood & Binney 2002). The star is released from this line when the spiral arm fades and the resonance weakens. If the star is trapped in a strong corotation resonance, then it can move far from the circular orbit curve along the Jacobi integral line. If it is released far from the circular orbit curve, then it is now in a non-circular orbit and will not get picked up by later spiral arm corotation resonances. Its radial migration history has ended.

On the other hand, if the star is released close to the circular orbit line, though at a changed L_z, then it is again in a near-circular orbit and can be picked up by later corotation resonances. Hence, the radial migration proceeds through a series of small steps in L_z from one near-circular orbit to the next. If this sequence of near-circular orbits is broken, the star is deposited in an eccentric orbit and stops migrating. Thus, stars can migrate far in many steps but only if they never stray far from circular orbits.

We therefore expect some metal-rich stars that have migrated out from the inner galaxy to be in eccentric orbits. They are the ones whose radial migration was derailed after a few steps by being released into an eccentric orbit. A succession of weak spiral arms would favour migration via small steps between near-circular orbits. One strong spiral arm could break the migration for some of the stars.

If this is right, then contrary to the prevailing paradigm, radial migration can lead to some heating, but at the expense of terminating the migration for the heated star. The energy for the heating comes from the spiral arms which in turn feed on the Galactic differential rotation. A star captured from a near-circular orbit and released far from the circular orbit curve in (E, L_z) has acquired an increased epicyclic amplitude (radial action) and a large change (positive or negative) in its angular momentum. There could be stars from the inner galaxy that now have $L_z > 1$ and large epicyclic amplitudes.

One mechanism that does not rely on transience was proposed by Minchev & Famaey (2010) and Minchev et al. (2011): this quasi-chaotic, unruly process results from interference between resonances from multiple rotating patterns, e.g. the central bar and the spiral arms which are known to rotate with different pattern speeds (cf. Brunetti, Chiappini & Pfenniger 2011). Jílková et al. (2012) and Quillen et al. (2018) investigate this resonance overlap and find that outward migration is possible but relatively inefficient. External influences can also drive radial migration, in particular, radial in-plane orbiting galaxies that come close enough to strongly perturb the disc (Quillen et al. 2009). Thus, the ratio of metal-rich

[5]In response to the question raised by Bland-Hawthorn, Krumholz & Freeman (2010), this argues that we should be looking inwards for members of the solar family, i.e. stars born in the same star cluster.

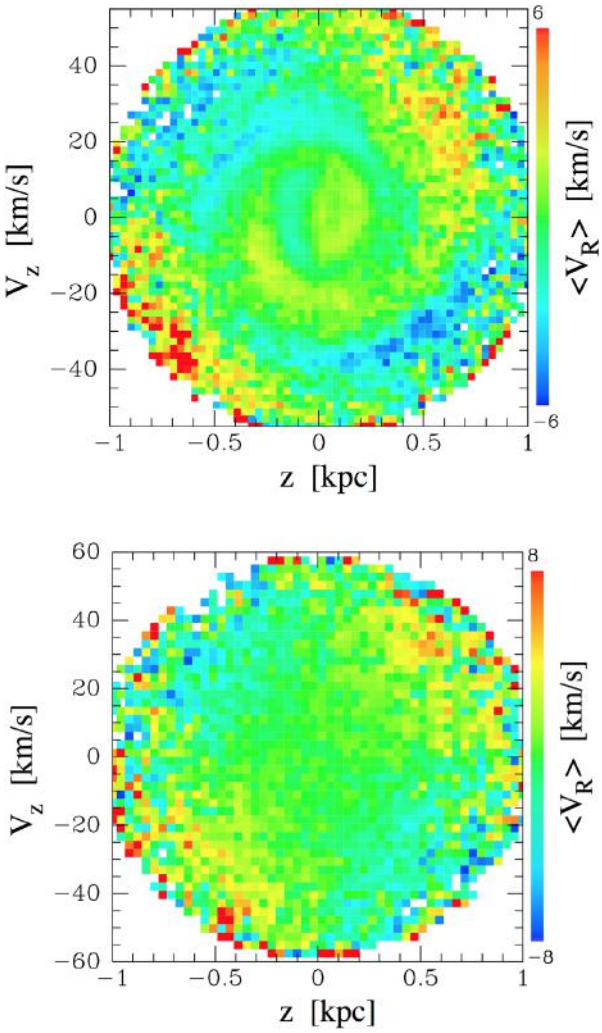

Figure 15. Top: $\langle V_R \rangle$ plotted in the zV_z phase plane over the original volume explored by Antoja et al. (2018). A quadrupole pattern (blue top left and bottom right, and red bottom left and top right) dominates the outer portion of the circle. Towards the centre, the spiral is clearly visible. Bottom: the simulated zV_z plane in a realistic axisymmetric model Galaxy (with no perturbing force) using 10^6 particles with sampling to match the *Gaia* selection function. The same quadrupole is apparent and arises because of the tilt of the velocity ellipsoid.

stars on radial compared to circular orbits in the local neighbourhood is a powerful constraint on the different transport mechanisms at play.

5 V_R AND THE VELOCITY ELLIPSOID

5.1 Tilt of the velocity ellipsoid

The top panel of Fig. 15 presents $\langle V_R \rangle$ in the zV_z phase plane as originally noted by Antoja et al. (2018). On the largest scale, a quadrupole pattern is evident, with $\langle V_R \rangle$ becoming small at top left and bottom right, and large at top right and bottom left. The bottom panel shows the structure of the zV_z plane in a realistic axisymmetric model Galaxy: the same quadrupole is evident, so the quadrupole is expected in a fully phase-mixed Galaxy.

The lower panel in Fig. 15 was created using the machinery described in Binney & Schönrich (2018) and the AGAMA software

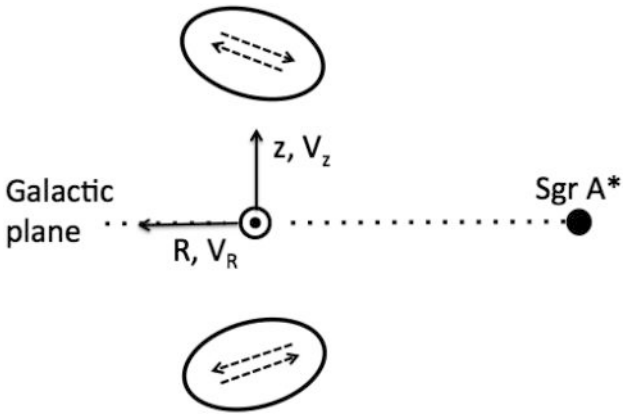

Figure 16. Left: the adopted coordinate frame in Galactic cylindrical coordinates shown with respect to the Sun's position. The tilted velocity ellipsoids above and below the Galactic plane are also indicated. The dashed arrows show the direction of the fastest motions within the ellipsoid. When viewed from the Sun, the velocity ellipsoids produce a characteristic quadrupole $\mp \pm$ pattern seen in the $\langle V_R(z, V_z) \rangle$ plane from the GALAH and *Gaia* data.

package (Vasiliev 2018). The dark matter, bulge, and stellar halo were each assigned a distribution function (DF) of the form $f(J)$ introduced by Posti et al. (2018). The thin and thick discs were assigned DFs $f(J)$ with forms that will be presented in an upcoming paper (Binney & Vasiliev, in preparation). For given values of the parameters in the DFs, the model's potential was solved for iteratively after adding the potential of the gas disc assumed by Piffl et al. (2014). The parameters in the DF were fitted to the *Gaia* DR2 sample via pseudo-data created by Monte Carlo sampling the model using a selection function that declines exponentially with distance from the Sun with a scale length of 500 pc, which is a simple approximation to the selection function of the Radial Velocity Spectrometer (RVS) sample. From these samples, velocity histograms were computed at 35 locations around the Sun and matched to the corresponding histograms for stars with parallax errors of 20 per cent or less. These Monte Carlo samples are used to construct the plot of $\langle V_R \rangle$ in the zV_z plane shown here.

Fig. 16 explains the connection between the quadrupole and the well-known tilt of the velocity ellipsoid as one goes above or below the plane: at $z = 0$, the long axis of the velocity ellipsoid lies in the Galactic plane. Off the plane, the long axis tips almost as much as is required for it to continue to point towards the Galactic Centre (Siebert et al. 2008; Binney et al. 2014). As a consequence, at locations above the plane, when a star is moving upwards (so it contributes to the upper right quadrant in Fig. 15), it is more likely to be moving outwards than inwards and averaging over stars we get red hues in Fig. 15. Conversely, at locations below the plane, an upwards moving star (contributing to the upper left quadrant of Fig. 15) is more likely to be moving outwards than inwards, and overall we have blue hues. Hence, the quadrupole shown by Fig. 15 in the *Gaia* DR2 stars is a novel signature of the velocity ellipsoid's tilt. It should have been anticipated but seems not to have been.

5.2 The spiral in V_R

The most prominent feature of Fig. 15 is a spiral observed in $\langle V_R(z, V_z) \rangle$ that is broadly similar to that in $\langle V_\phi \rangle$ (Figs 6 and 7). In detail, the spirals differ: near the centre, the V_R spiral is less tightly wound than the V_ϕ spiral. In Fig. 17, we dissect the plane

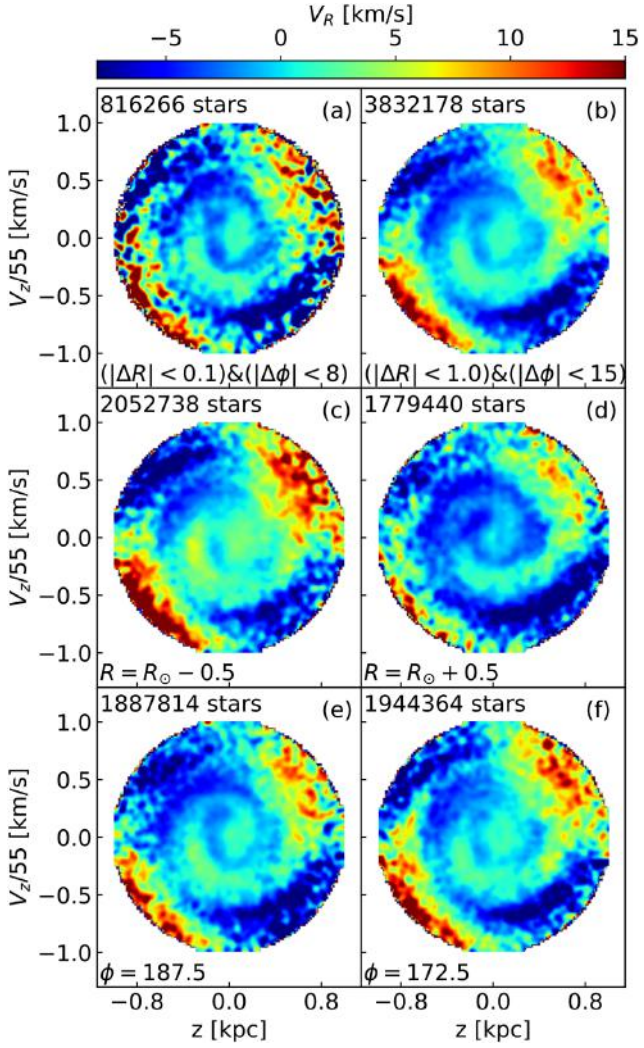

Figure 17. Map of median V_R in (z, V_z) plane for stars in the solar neighbourhood using data from *Gaia* DR2. The sample definitions are the same as in Fig. 8. The quadrupole defined by the sign changes in each quadrant are due to the tilt of the velocity ellipsoid (see the sketch in Fig. 16). Note that a weak phase spiral pattern is visible in the centre. The pattern is stronger for the $R = R_0 - 0.5$ case than for the $R = R_0 + 0.5$ case. (ϕ is quoted in degrees.)

along the same lines as Fig. 8. Once again, the V_R spiral pattern in Antoja's original volume (a) is recovered in the 20× larger GALAH volume in (b). Interestingly, the inner spiral does not vary greatly with location, either in radius (c) and (d) or in azimuth (e) and (f). But the quadrupole pattern is substantially stronger over the inner disc compared to the outer disc; there is no gradient in azimuth. These are real variations as reflected in the matched star counts in each panel.

In Fig. 18, we use the GALAH data to dissect the phase spiral in V_R by chemistry. The quadrupole pattern is evident in all panels and tends to obscure the phase spiral. The latter is most evident in the panel for the summed α-poor disc (b). Thus, the spiral in $\langle V_R \rangle$ is manifested in the same populations as the spiral in $\langle V_\phi \rangle$ as we would expect if it is simply another aspect of a common dynamical phenomenon (Binney & Schönrich 2018).

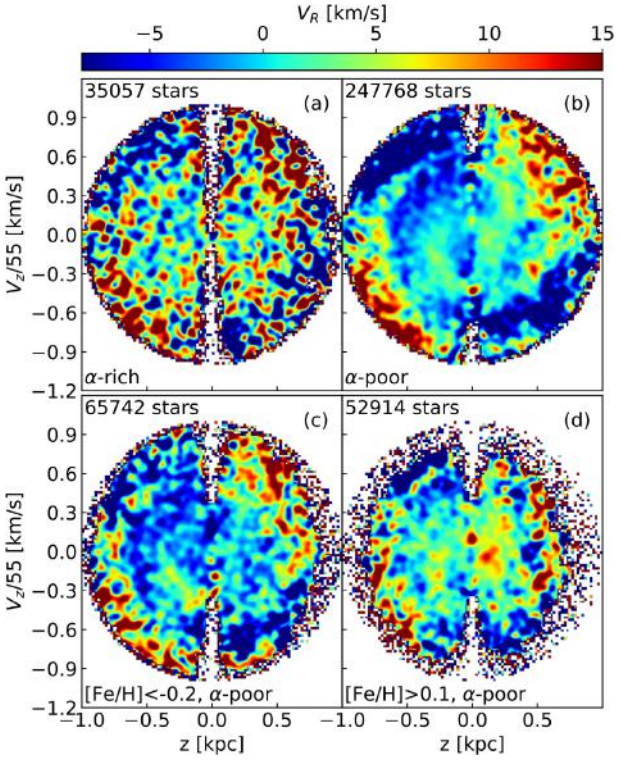

Figure 18. Map of median V_R in (z, V_z) plane for stars in the solar neighbourhood using data from GALAH and *Gaia* DR2. The sample definitions are the same as in Fig. 10.

6 DYNAMICAL INTERPRETATION

6.1 Departures from equilibrium

In Sections 4 and 5, we encountered abundant evidence that the phase spiral is present over a wide extent in radius and involves stars of many ages and chemical compositions. Hence, it definitely does not arise through phase mixing of stars born in a massive starburst (Candlish et al. 2014). Rather it is an extension to the zV_z plane of one of the most important discoveries in *Hipparcos* data: the detection by Dehnen (1998) of clumps in the *UV* plane. The traditional explanation of such 'star streams' is that they are dissolving star clusters, but from the work of Dehnen (1998) and Famaey et al. (2005), it became clear that the clumps in the *UV* plane were heterogeneous in age and metallicity so they could not comprise stars that formed together, but must have been swept up by some dynamical process. The GALAH data establish that the stars that make up the zV_z spiral do not have a common origin but have been likewise caught up in a dynamical process.

In addition to the in-plane clumps, early evidence for departures from equilibrium came from the Galactic outer disc. Here, warps, rings and ripples are observed (e.g. Newberg et al. 2002; Rocha-Pinto et al. 2004; Newberg et al. 2007) and these have been interpreted in terms of corrugations and waves triggered by a passing satellite (e.g. Quillen et al. 2009; Purcell et al. 2011; Widrow et al. 2012; Gómez et al. 2013; de la Vega et al. 2015). These also manifest as kinematic (Widrow et al. 2012; Williams et al. 2013; Carlin et al. 2013) and density asymmetries (Yanny & Gardner 2013; Slater et al. 2014; Xu et al. 2015) above and below the Galactic plane. While most authors conclude that the wave-like patterns can be triggered by a massive perturber like the Sgr dwarf (cf. Elmegreen et al. 1995),

none of the models predicted the 'phase spiral' discovered by Antoja et al. (2018) that are a natural consequence of the disturbance, as we discuss.

6.2 Perturber models

To a first approximation, the Galactic disc is an axisymmetric equilibrium structure. The data now at hand force us to move on from this starting point to consider the effects on non-axisymmetric and non-stationary perturbations.

The earlier perturber models provided the context for interpreting the *Gaia* discovery. Antoja et al. (2018) show examples of an initial clump of stars in the zV_z plane winding up into a phase spiral as they move in a toy anharmonic potential $\Phi(z) = az^2 + bz^4$. Binney & Schönrich (2018) pointed out that this model does not explain why the spiral is weak in a plot of the density of *Gaia* DR2 stars in the zV_z plane but emerges clearly when $\langle V_\phi \rangle$ is plotted. They argued that the keys to understanding this phenomenon are (i) that Ω_z is a strong function of L_z as well as of J_z so stars are sorted by L_z as they progress around the zV_z plane, and (ii) that when an intruder such as the Sgr dwarf crosses the plane, oscillations are initialized in both the in-plane and perpendicular directions. That is, in the Antoja model, the observed spiral is the result of *two independent but synchronized oscillations*.

Binney & Schönrich (2018) presented a toy model of the impact of an intruder crossing the disc. They made the model tractable by using the impulse approximation to compute the disturbance that the intruder causes. While recognizing that the impulse approximation would in this case be invalid, they argued that errors introduced by it are smaller than those introduced by neglect of the perturbations to the Galaxy's gravitational potential that arise as the disc responds to its initial stimulus. Notwithstanding its weaknesses, their toy model reproduced for the first time spirals in $\langle V_\phi \rangle$ and $\langle V_R \rangle$ with plausible parameters for the mass and location of the intruder.

The deficiencies of the perturbative treatment cannot be addressed until there is a major breakthrough in the theory of disc dynamics. It is intuitively clear that if we could solve the equations of linearized perturbation for a self-gravitating stellar disc, at least two wave modes would emerge: in one mode, the disturbance would be largely parallel to the plane and be associated with spiral structure, and in the other mode, the perturbation would be largely perpendicular to the plane and would be associated with warps and corrugation waves.

6.3 Revisiting disc dynamics

After decades of frustration, we now have in the work of Goldreich & Lynden-Bell (1965), Toomre (1969, 1981), Sellwood & Carlberg (2014), and Fouvry et al. (2015) a convincing theory of the dynamics of razor-thin discs. Noise from any source, including Poisson noise, generates leading spiral waves, which are swing amplified near their corotation resonance and subsequently absorbed by Landau damping at a Lindblad resonance. The disc is heated by the absorption in an annulus that is typically very narrow, and as a consequence the impedance of the disc to propagating spiral waves is caused to vary on small scales. When a wave propagating from its corotation to its Lindblad resonance subsequently hits such a region, it is partially reflected back to corotation to be re-amplified. Gradually, as the disc ages and the number of these narrow regions grows, significant fractions of swing-amplified waves are reflected by some feature back to corotation to be re-amplified before they can reach their Lindblad resonance and be absorbed. Hence, the disc's responsiveness to stimulation by noise steadily grows until the disc becomes simply unstable. At that point, the spiral structure becomes an O(1) phenomenon and a bar forms.

The picture just described certainly marks a significant step forward in understanding galaxies, but it falls short of what is required to address the data we now have because it is confined to razor-thin discs. It is clear that the fundamentally in-plane mode must involve V_z in addition to V_ϕ because stars will be drawn down to regions of high density (Masset & Tagger 1997). That is, a propagating spiral arm will force oscillations perpendicular to the disc that satisfy the symmetry condition $\langle V_z(-z) \rangle = -\langle V_z(z) \rangle$. These motions will remain conjectural until the theory of spiral structure has been extended from razor-thin discs, in which vertical motion is impossible, to discs of finite thickness; this extension proves extremely difficult (Fouvry et al. 2017).

The available formalism relating to the second kind of mode, corrugation waves, is even more primitive than the current theory of spiral structure because it involves neglecting epicyclic oscillations in addition to taking the disc to be razor thin (Hunter & Toomre 1969). Hence, we really have very little idea what a proper theory of corrugation waves would look like. We do, however, know that their z-motions would satisfy the symmetry condition $\langle V_z(-z) \rangle = \langle V_z(z) \rangle$ and they will almost certainly involve V_ϕ in addition to V_z because warps are all about torques exerted by one ring on another.

In these circumstances, the natural thing to do is to resort to N-body simulation. As we shall see, modelling the *Gaia* DR2 data in this way is extremely challenging because one needs to achieve high resolution in the small part of the 6D phase space in which the spiral is detected, while at the same time resolving the dynamic (live) dark halo, which we expect to participate in the excitations under study (Binney, Jiang & Dutta 1998) and extends to beyond 100 kpc, sufficiently to prevent it becoming an important source of artificial Poisson noise.

We now revisit recent work on Sgr's interaction with the Galactic disc by carrying out a new suite of simulations. Our goal is to understand how the phase spiral can inform us of when this event happened, and how the disturbance was able to propagate through the disc. We consider the different disc response to a purely impulsive interaction (high speed and hyperbolic orbit) and the multicrossing 'trefoil' orbit of the Sgr dwarf.

7 *N*-BODY SIMULATIONS

In a recent paper, Tepper-García & Bland-Hawthorn (2018) examine the impact of Sgr on the Galaxy with an N-body, hydrodynamical simulation that has the unique feature of including a gas component demanded by the resolved star formation history of the dwarf. This work, which used the adaptive mesh refinement gravito-hydrodynamics code RAMSES (version 3.0 of the code described by Teyssier 2002), emphasized that the number of disc crossings and the timing of Sgr's orbit depend on the rate at which Sgr loses dark and baryonic mass. Here, we rerun these models without the gas component using an updated Galaxy model (Table 1) with extended ranges of intruder mass and orbit parameters (Table 2). Our simulations contain almost three million particles, of which 1.6 million are disc stars and one million are dark-matter particles.

We include a simulation of an unperturbed disc to emphasize the long-term stability of our models. In addition to the realistic Sgr orbit models with their multiple crossings, we also simulate intruders crossing the disc along (unrealistic) hyperbolic orbits to study the disc's response to a strong, one-time impulsive transit. The face-on projection of both orbits shown in Fig. 19 suggests

Table 1. Galaxy model parameters. Column headers are as follows: M_t = total mass (10^9 $M_\odot$); r_s = scale length (kpc); r_{tr} = truncation radius (kpc); and N_p = number of particles (10^5).

Galaxy	Profile	M_t	r_s	r_{tr}	N_p
DM halo	H	10^3	38.4	250	10
Bulge	H	9	0.7	4	3
Thick disc	MN	20	5.0[a]	20	6
Thin disc	Exp/Sech	28	5.0[b]	20	10

Notes. H: = Hernquist (1990) profile; MN: = Miyamoto & Nagai (1975) profile; Exp:= radial exponential profile.; Sech: = vertical $\mathrm{sech}^2 z$ profile.
[a]Scale height set to 0.5 kpc.
[b]Scale height set to 0.3 kpc.

Table 2. Overview of intruder models. Column headers are as follows: M_{tot} = total mass (10^9 $M_\odot$); M_{tid} = tidal mass (10^9 $M_\odot$); r_{tr} = truncation radius (kpc); and N_p = number of particles (10^5). The last column gives the approximate initial orbital speed (km s^{-1}). See the notes below the table for more information.

Model	M_{tot}	M_{tid}	r_{tr}	N_p	v_0
K (high mass, Sgr orbit)	100	90	60	5	80
L (intermediate mass, Sgr orbit)	50	40	45	5	80
M (low mass, Sgr orbit)	10	7	25	5	80
R (high mass, one transit)	100	60	24	2	370
S (intermediate mass, one transit)	50	30	19	1	360
T (low mass, one transit)	10	5	12	1	350

that with the realistic orbit successive crossings may influence the coherence and longevity of the phase spiral.

Appendix A summarizes the content of movies of these simulations that are available at http://www.physics.usyd.edu.au/galah_exp/sp. There are movies to show both configuration space and phase space. We practice an open policy on set-up files for all of our *N*-body + MHD studies to encourage cross-checking, and encourage others to do the same.

Below we provide plots in the zV_z phase plane for particles that are widely distributed in L_z. Fig. 20 helps us to understand the basic structure of these plots. Its top six panels show curves of constant J_z in the zV_z plane for orbits with circular angular momentum and small radial action at radii that decrease from $R = 20$ kpc at top left to $R = 5$ kpc at bottom right. The values of J_z for which curves are plotted are the same in each panel. As one moves inwards, the curves become steadily more elongated vertically, while their area, which is equal to $2\pi J_z$, remains constant because the set of J_z values is the same in every panel. These orbit traces stretch along the V_z axis, while shrinking along the z-axis in consequence of growth in the vertical restoring force K_z as R decreases and the surface density of the disc increases. The lower six panels of Fig. 20 show the extent of phase wrapping in a given time (250 Myr). As R shrinks, Ω_z increases and an initially radially directed straight line in the phase-plane wraps more tightly in a given time.

7.1 Set-up

The simulations' axisymmetric initial conditions were assigned by the technique of Springel, Di Matteo & Hernquist (2005) as implemented in the DICE code (Perret et al. 2014). This technique imposes $\sigma_R = \sigma_z$ and in parts of the disc σ_R fell below the value that makes Toomre's (1964) stability parameter

$$Q_\star \equiv \frac{\sigma_R\,\kappa}{3.36\,G\,\Sigma_\star} = 1.5, \tag{8}$$

where κ and $\Sigma_\star$ are the epicyclic frequency and stellar surface density. Where $Q_\star < 1.5$, we increased σ_R (but not σ_ϕ) to ensure $Q_\star \geq 1.5$ everywhere. Since the initial conditions are for a system slightly out of equilibrium, each simulation was evolved for roughly 4 Gyr before being disturbed. We refer to the model after this relaxation phase as the 'unperturbed' model (Model P). See Table 1 for details of this model Galaxy,

We disturbed this model in six simulations. The intruders had masses of 1, 5, or $10 \times 10^{10} M_\odot$ and comprised a $4 \times 10^8 M_\odot$ stellar system embedded in a dark halo. Both the stellar system and the dark halo were truncated Hernquist spheres. Their scale radii were 0.85 and 10 kpc, respectively. The stellar system was truncated at 2.5 kpc, while the truncation radius of the dark halo is listed in Table 2. A simulation with each of these masses was started with the intruder at $(R, z) = (21, 45)$ kpc on a hyperbolic orbit of eccentricity $e = 1.3$ and pericentre distance 10 kpc. For each intruder mass, a second simulation was started with the intruder located 125 kpc from the Galactic Centre on a 'trefoil' orbit of the type that roughly fits observations of the Sgr dwarf (see Tepper-García & Bland-Hawthorn 2018, and Fig. 19). The intruder's tidal radius was set appropriate to a Galactocentric distance of 50 kpc in the case of a hyperbolic orbit and a distance 125 kpc in the case of a trefoil orbit. The simulations with trefoil orbits are labelled K, L, and M, while those with hyperbolic orbits are labelled R, S, and T. In the most realistic simulation (Model K), the first and second pericentric passages occurred ∼2.5 and ∼1 Gyr ago, while the last passage occurred 420 Myr ago, consistent with observations (Ibata et al. 1997).

7.2 Hyperbolic encounters

In simulations R, S, and T with an intruder on a hyperbolic orbit, at $t \sim 95$ Myr, the disc moves up towards the approaching intruder and its centre of mass experiences a recoil. Figs 22 and 23 show, for the high- and intermediate-mass intruders respectively, the disc in real space (panels a and b) and in the zV_z phase plane (lower panels) at this time. Numerous signs of disequilibrium are evident in all panels of both figures. In the top panels, we see clear $m = 1$ asymmetry, including a couple of distinct spiral arms, and variations in $\langle V_\phi \rangle$ that have much larger amplitude than those found in the unperturbed simulation P1. These variations seem to be associated with corrugation waves moving through the disc. In the middle, phase-plane, panels, wisps can be identified that might be part of phase spirals. It is remarkable that there are such features, since these figures include particles irrespective of their azimuth or Galactocentric radius, and it is to be expected that different patterns at widely differing azimuths and radii would wash each other out more completely than they do. Plots that are restricted in radius and azimuth lack the resolution required to trace the spiral.

By $t \sim 130$ Myr, as the intruder crosses the plane at $R \sim 13$ kpc, the entire disc has been shaken. By $t \sim 180$ Myr, the interaction has generated a spiral arm and a strong warp in the outer disc that precesses around the disc (cf. Gómez et al. 2015). The disc does not begin to fall back down towards the receding intruder until after $t \sim 400$ Myr. The disc is strongly forced by the intruder's tidal field for only ∼100 Myr but its response persists for the 2 Gyr duration of the simulation.

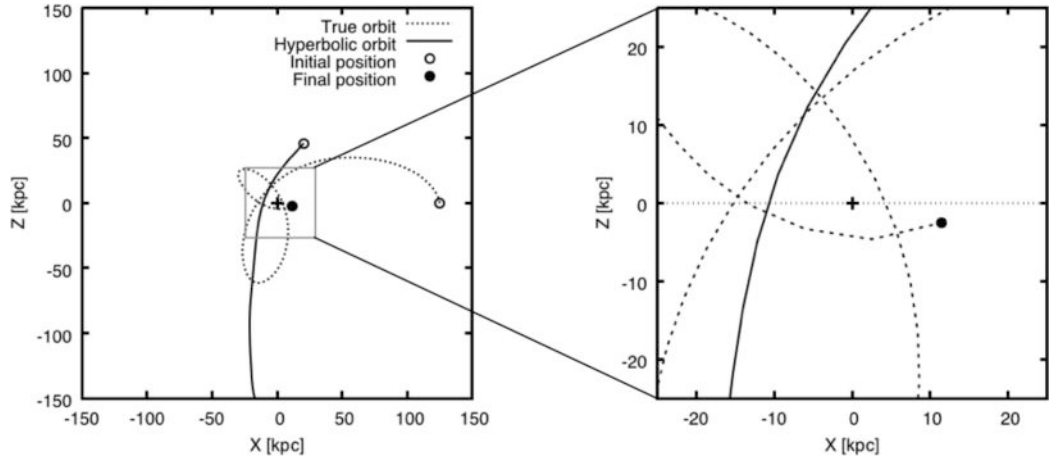

Figure 19. The projection of the polar orbits for the intruders with different mass (hyperbolic versus true) into the (x, y) plane seen from the NGP. The cross indicates the Galactic Centre. The dashed line shows the complex 'trefoil' orbit of Sgr over the past 2.3 Gyr, now accepted across many studies since Law, Johnston & Majewski (2005). Sgr (shown as a filled circle) crossed the disc about 420 Myr ago at $R = 13$ kpc and is due to transit again in about 50 Myr. The inset magnifies the central region. For more details, see Tepper-García & Bland-Hawthorn (2018).

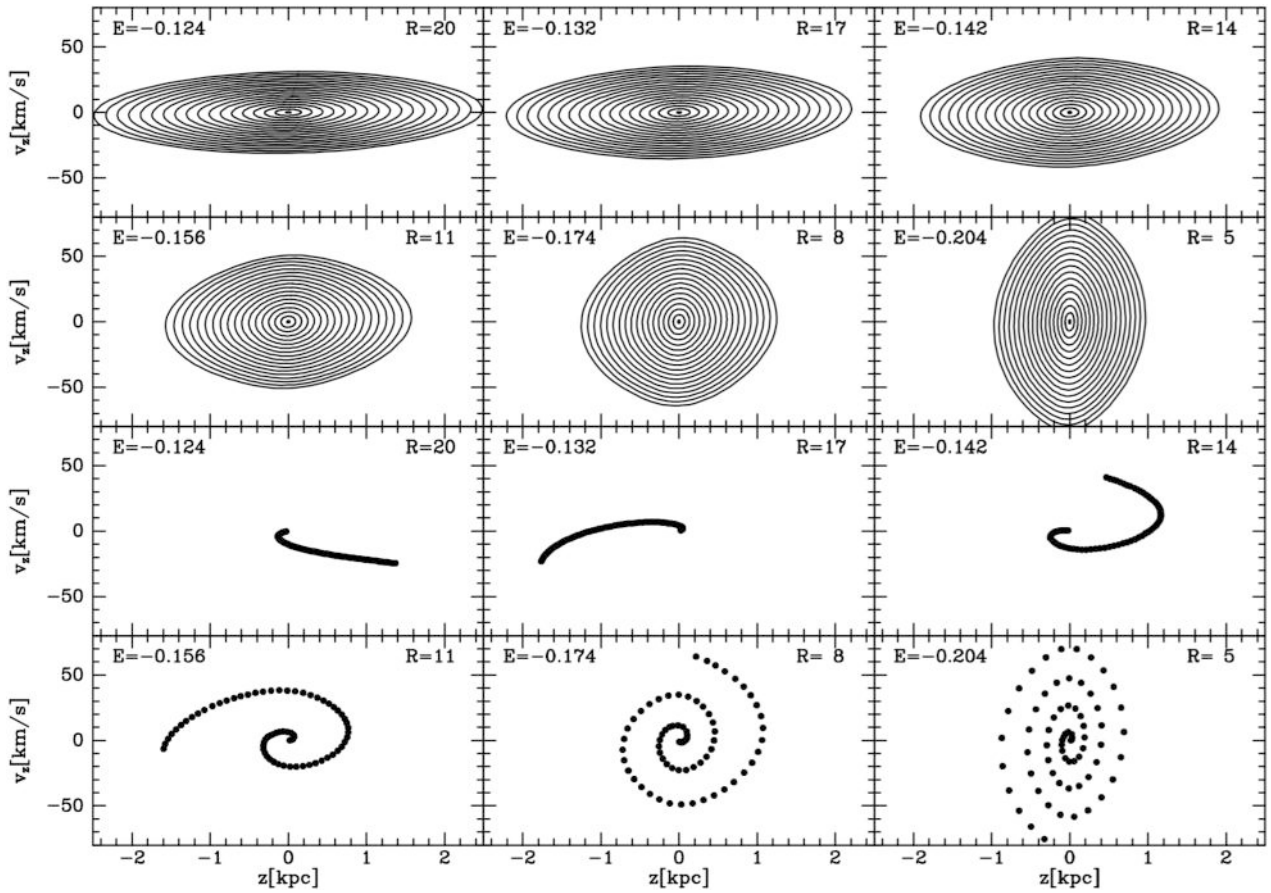

Figure 20. The top six panels show surfaces of section in the vertical phase plane (z, V_z) at six different radii ($R = 20$, 17, 14, 11, 8, and 5 kpc) which are chosen to match the radial extent of our new disc simulations and the *Gaia*/GALAH study. The panels were computed with the AGAMA software package (Vasiliev 2018) adopting the Galactic potential from Piffl et al. (2014). The amplitude of the outer ellipse and the phase spiral at $R = 8$ kpc are chosen to match the *Gaia* data. In every panel, the outermost ellipse has the same area ($=2\pi J_z$) and the orbital energies E are indicated. The J_z values for each concentric ellipse moving outwards are: 0.008, 0.20, 0.65, 1.35, 2.31, 3.52, 4.99, 6.71, 8.69, 10.93, 13.42, 16.17, 19.17, 22.43, 25.94, 29.71, 33.73, and 38.01 kpc km s^{-1}. In the outer disc, the ellipses elongate in z because stars travel farther and slower in the weaker disc potential. All orbits have radial action $J_R = 0.01$ kpc^2 Myr^{-1} $= 9.78$ kpc km s^{-1} and J_ϕ for the circular orbit at the quoted radius. The bottom six panels coincide with the panels above indicated by the total energies; these reveal the impact of phase wrapping after 250 Myr where all points are initially lined up along the $z < 0$, $V_z = 0$ axis. Across the inner disc, the stronger disc gravity leads to faster vertical oscillations which result in faster phase wrapping.

7.3 Realistic orbit

Contemporary models agree that Sgr initially crossed the disc along a trajectory perpendicular ($i \sim 90^\circ$) to the Galactic plane (e.g. Law et al. 2005; Purcell et al. 2011), but at late times, as the orbit became circularized by dynamical friction (e.g. Jiang & Binney 2000), the trajectory evolved to one that makes a smaller angle with the disc ($i \lesssim 30^\circ$). As a result of both this change in inclination and the shrinking of the orbit's semimajor axis, passages through the disc became steadily less impulsive. The most recent passage occurred at a radius of about $R \approx 13$ kpc.

The left-hand panels of Fig. 24 show for Model K the real space (top two panels) and the phase plane (bottom panel) at $t = 1.77$ Gyr, which is 30 Myr before the high-mass intruder crossed the plane. The right-hand panels show the same spaces 90 Myr after the transit. In the bottom left panel showing the phase plane prior to the passage, a phase spiral can be discerned that has vanished from the bottom right panel for the moment after the passage. Closer examination of the data plotted in the bottom left panel of Fig. 24 reveals three distinct phase spiral patterns arising in three radial bins ($R = 17$, 15, and 12 kpc) and their axis ratios vary in line with the predictions of Fig. 20. The Movie K3 shows that a spiral re-appears as the simulation progresses, so our simulations are consistent with the observed spiral being generated ∼400 Myr ago as Antoja et al. (2018) and Binney & Schönrich (2018) suggested.

We can gain insight into the total (rather than stellar) mass of the Sgr dwarf by combining the simulations with *Gaia* DR2. The low-mass intruder on a realistic orbit (Model M) barely ruffles the disc. The high-mass intruder (Model K), by contrast, produces features with $|z_{\rm max}| \lesssim 5$ kpc and $|V_{z_{\rm max}}| \lesssim 50$ km s^{-1} that exceed the scale of the *Gaia* features. The intermediate-mass intruder produces disequilibria of about the required amplitude at $R = R_0$. This is consistent with the finding of Binney & Schönrich (2018), who generated a realistic spiral with an intruder of mass 2×10^{10}M$_\odot$ and an impact parameter of $R = 20$ kpc.

8 CONCLUSIONS

8.1 Summary

We have used the data from the second releases of the *Gaia* and GALAH surveys to examine the Galactic discs in a sphere of radius ∼1 kpc around the Sun. The GALAH survey allows us to divide the disc into its two fundamental components, the α-rich and the α-poor discs. Traditionally, these have been called the thick and thin discs but it is now clear that this terminology can be confusing.

The α-rich disc is old and largely confined to within R_0. We have shown that its velocity dispersion tensor has a bias towards V_z that is unique in the Galaxy. Although the α-rich disc must have formed rather quickly (and before the α-poor disc started to form), it has a complex internal structure, with its more metal-poor stars being on highly eccentric, low-angular-momentum orbits.

The α-poor disc is the accumulation of up to 10 Gyr of gradually declining star formation. Its history has bequeathed it a complex internal structure that differs from that of the α-rich disc in two key respects: (i) stars with less angular momentum tend to be more rather than less metal-rich; (ii) its stars have larger rather than smaller in-plane velocity dispersions than the dispersion perpendicular to the plane.

Following the discovery by Antoja et al. (2018) of a phase spiral when $\langle V_\phi \rangle$ is plotted in the zV_z phase plane, we have used *Gaia* and GALAH to examine this plane closely. In this plane, stars move on ovals whose area is proportional to the vertical action J_z. Hence, α-rich stars are widely dispersed in the zV_z plane, whereas α-poor stars become less widely dispersed as [Fe/H] decreases. On account of asymmetric drift, $\langle V_\phi \rangle$ decreases as one moves away from the centre of the zV_z plane. On top of this systematic decrease, a spiral is evident in $\langle V_\phi \rangle$ that can be fitted with remarkable accuracy by a Archimedean spiral. Whereas Antoja et al. (2018) extracted the spiral from *Gaia* data for stars that lie in thin cylindrical shell around the Sun, we find that a spiral remains prominent and remarkably invariant when this volume is greatly enlarged and shifted in radius or in azimuth. These findings suggest that the spiral is a global feature of the disc as it would be if it were excited by a massive halo substructure, particularly in view of the extensive earlier work on warps and ripples in the outer disc.

While the general form of the phase spiral is conserved across the different slices (correcting for the variable aspect ratio), the GALAH data reveal changes in the 'contrast' (i.e. how well defined the spiral is against the background) in sections along the spiral when the data are sliced by stellar age, action, elemental abundance, or location. The inner spiral is better defined with stars younger than 3 Gyr and more metal rich ([Fe/H]>0.1). In Section 4.5, we discussed this result in the context of stellar migration.

The outer spiral is better defined in older, more metal-poor, α-poor stars. There are variations in the phase spiral contrast (coherence) with azimuth and radius. The spiral is hard to discern in the plot for α-rich stars. In Section 6.1, we discussed these results in the context of a disc corrugation that is mostly confined to the flaring α-poor disc. The spiral can be seen in LAMOST data, but these data do not allow detailed study because the phase spiral has low contrast and the latest data release does not include [α/Fe]. The spiral is clearest in stars with less than the median value of J_R. It is somewhat tighter in stars with smaller L_z as one expects from the tendency of the frequency Ω_z of motion in the zV_z plane to increase as L_z decreases.

8.2 The Galactic disc revisited

In Fig. 21, we provide a sketch of the corrugated disc that we believe to be consistent with the work above. This simple schematic is remarkably successful in explaining most of the features we see in the GALAH/*Gaia* analysis. Recall that the outer part of the spiral (large $r_{\rm ps}$) is strongest in old (Figs 14c and d), metal-poor stars (Fig. 10c). It is also more prominent at larger Galactocentric radius (Figs 8c and d), and more evident in the α-poor disc compared to the α-rich disc (Figs 10a and b). It also appears stronger at lower ϕ (Figs 8e and f) presumably because these corrugations are not purely radial waves, but exhibit a degree of spirality. We also note that it is stronger for $L_z > 1$, consistent with being more prominent outside of the Solar Circle (Fig. 11c). That so many independent data can be marshalled in this way demonstrates the power of combining *Gaia* data with detailed stellar chemistry from ground-based surveys.

A clear example of a corrugated disc observed in both gas and stars is seen in the 'superthin' Sd galaxy IC 2233 at a distance of about 10 Mpc (Matthews & Uson 2008a,b). The undulations are seen in the spatial offsets of the gas and young stars, and kinematically in the cool and warm gas. There are parallels with what we observe in the Galaxy. Interestingly, the undulation effect is weaker in the old stellar population. Moreover, the wavelength (≈7 kpc) and amplitude (≈150 pc) of the corrugation (see fig. 1 in Matthews & Uson 2008b) are remarkably similar to the same scale lengths observed in the Galaxy (cf. fig. 18 in Xu et al. 2015), *and* they determine that the corrugation amplitude grows with increasing

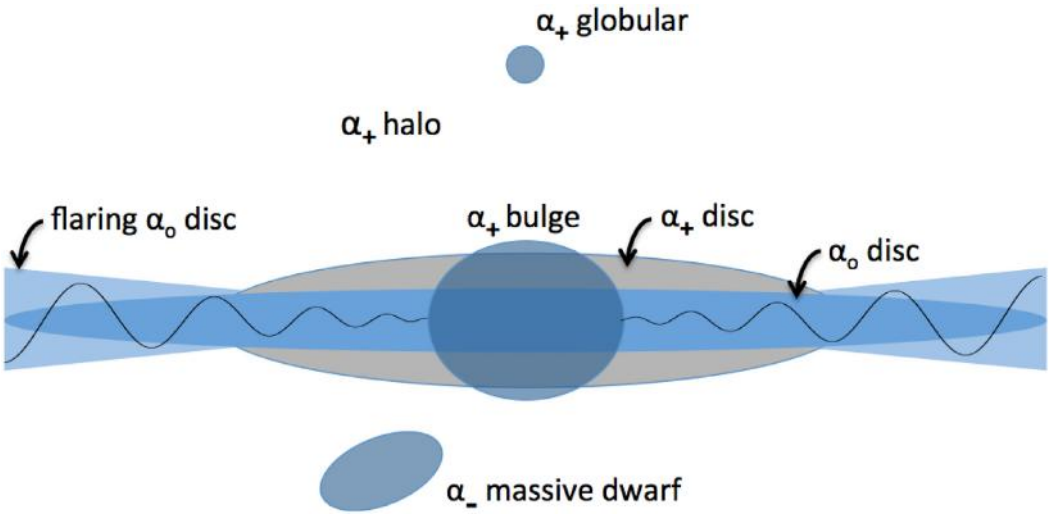

Figure 21. A sketch of the corrugated disc that brings together much of what is learnt from the GALAH/*Gaia* analysis. We also illustrate the use of the new α notation discussed in Section 2.1. The wave propagation gives rise to the phase spiral. As models show (Section 6.1), the corrugation amplitudes grow in $|z|$ with increasing radius. This can be understood in the context of the increasing vertical phase amplitude with R in Fig. 20. Thus, the corrugation is mostly confined to the α_o disc at all radii. This behaviour is also observed in external galaxies (see Section 8.2).

radius, as we do for the Galaxy. At a fixed oscillation energy, the increasing sinusoidal amplitude of the oscillation with radius, and its anticorrelation with the sinusoidal velocity amplitude (Matthews & Uson 2008b), are well explained by what we learnt from Fig. 20.

Do such corrugations exist in the HI gas of the Milky Way? As far as we can tell, this has not been found locally in recent surveys (Kalberla & Kerp 2009), but there may be evidence for such behaviour at other radii (e.g. Lockman 2002). It is tempting to suggest that the tilt of the widely discussed 'Gould's belt' of star formation (Zari et al. 2018) in the local disc is somehow indicative of a local disc corrugation, by analogy with IC 2233 and other galaxies listed by Matthews & Uson (2008b).

8.3 Dynamical time-scale

The inferred dynamical time-scale for the phase spiral depends critically on the adopted disc potential. In our final analysis, we adopt the disc potential of Piffl et al. (2014) because this was constrained to fit the well-established, vertical density profile through the Sun's position (Gilmore & Reid 1983). When angle-action coordinates are used to plot the zV_z phase plane, a spiral is evident that coincides well with the curve formed after 390 Myr by points that start from a common value of the angle variable θ_z. In contrast, when we adopt the Galactic potential from McMillan (2011), the inferred time-scale is 30 per cent higher (515 Myr). This suggests that the spiral is a relic of a disturbance the disc experienced about 400–500 Myr ago, in line with the numerical simulations.

In Section 5.1, a plot of $\langle V_R \rangle$ in the zV_z plane proves to be a superposition of two features: a spiral that is very similar to that seen in the plot for V_ϕ superposed on a quadrupole pattern that we have traced to the morphology of orbits in the Rz meridional plane and the well-known tilting of the velocity ellipsoid as one moves away from the plane. The results summarized here establish that the spiral is not associated with the dispersal of stars from their natal location but, like the structure *Hipparcos* revealed in the *UV* plane, has arisen through some dynamical process disturbing the Galaxy's equilibrium.

A strong case has been made by Antoja et al. (2018) and Binney & Schönrich (2018) that the spiral is a consequence of the tidal pull of the Galaxy by a halo substructure, possibly the Sgr dwarf, as it crossed the plane ∼0.5 Gyr ago. Binney & Schönrich (2018) simulated this process using two undesirable approximations: that the event was impulsive and that it does not modify the Galaxy's gravitational field. Currently, these approximations can only be lifted by doing a full N-body simulation of the event.

In Section 7 and the Appendix, we show results from six such simulations. Even with three million particles, we did not achieve sufficient resolution in an equivalent GALAH volume to reveal the phase spiral locally (i.e. within a few hundred parsecs), as others have claimed with an order of magnitude more particles (Laporte et al. 2019). Instead, we populate the zV_z plane with all stars in a simulation, thus effectively superposing phase planes at all azimuths and many different radii.

Remarkably, in light of this superposition, for intruders of mass 3×10^{10} $M_\odot$ and above (stripped down from a higher mass), spiral-like 'features' that are consistent with being phase spirals can still be identified in the simulated phase plane. These structures lie outside R_0, and reach to greater distances from the plane and larger values of $|v_z|$ than the observed spiral. An intruder of mass 10^{10} $M_\odot$ stripped down to 5×10^9 $M_\odot$ does not perturb the disc enough to generate measurable phase-plane structure, so we conclude that the observed structure was generated by a body of greater mass. This conclusion is consistent with the findings of Binney & Schönrich (2018) and Laporte et al. (2019).

Our new simulations reveal the full nature of the interaction between the Galaxy and the infalling, shredding, multitransiting dwarf consistent with the well established 'trefoil' orbit of the perturber. The details of this interaction are crucial. Our simulations are significant in predicting the large-scale patterns of a corrugated disc that are now revealed in the data (Khanna et al., in preparation). The simulations reveal phase spirals co-existing at different radii due to the disc corrugation, with varying zV_z aspect ratios in line with Fig. 20. The simulations also reveal for the first time that the subsequent disc crossings destroy the phase spiral coherence, such

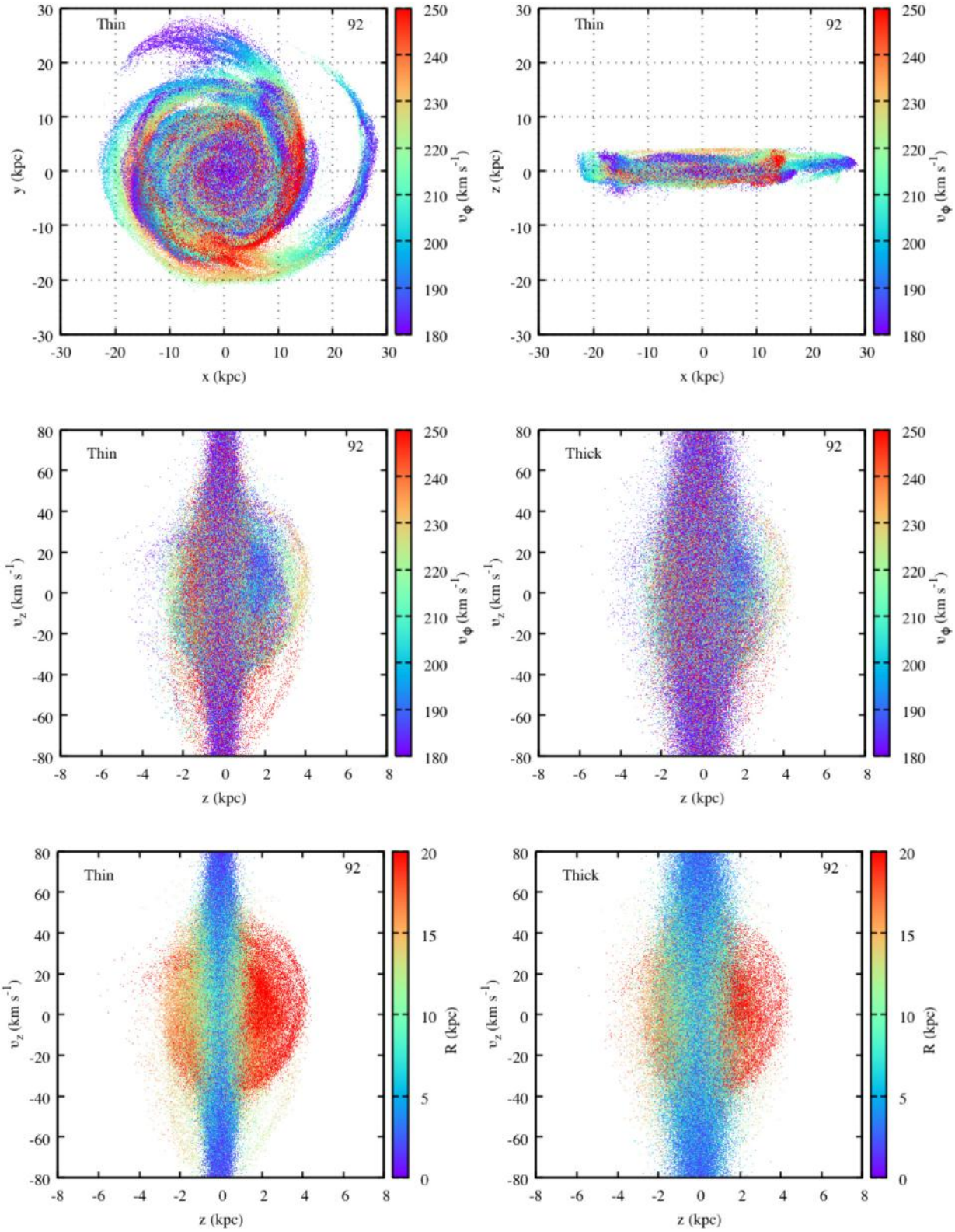

Figure 22. Simulation of a high-mass intruder (Model R; Table 2) on a hyperbolic orbit where only the Galaxy is shown. (a) *xy* plane for the thin disc where the particles are colour coded with V_ϕ (Movie R2). (b) *xz* plane for the thin disc where the particles are colour coded with V_ϕ (Movie R2). (c) zV_z phase plane for the thin disc colour coded with V_ϕ (Movie R3). (d) zV_z phase plane for the thick disc colour coded with V_ϕ (Movie R3). (e) zV_z phase plane for the thin disc colour coded with R (Movie R4). (f) zV_z phase plane for the thick disc colour coded with R (Movie R4). Note the coherent V_ϕ velocity structures, especially in configuration space and their interrelation across all phase planes, mostly due to strong V_z and weaker V_R motions. The thick disc shows the same extent and structure as the thin disc if one allows for order of magnitude fewer particles. In the vertical phase plane $V_\phi(z, V_z)$ in (c) and (e), there are coherent one-armed phase structures occurring at the same time ($t = 92$ Myr) near 20 kpc (red) and 10 kpc (green).

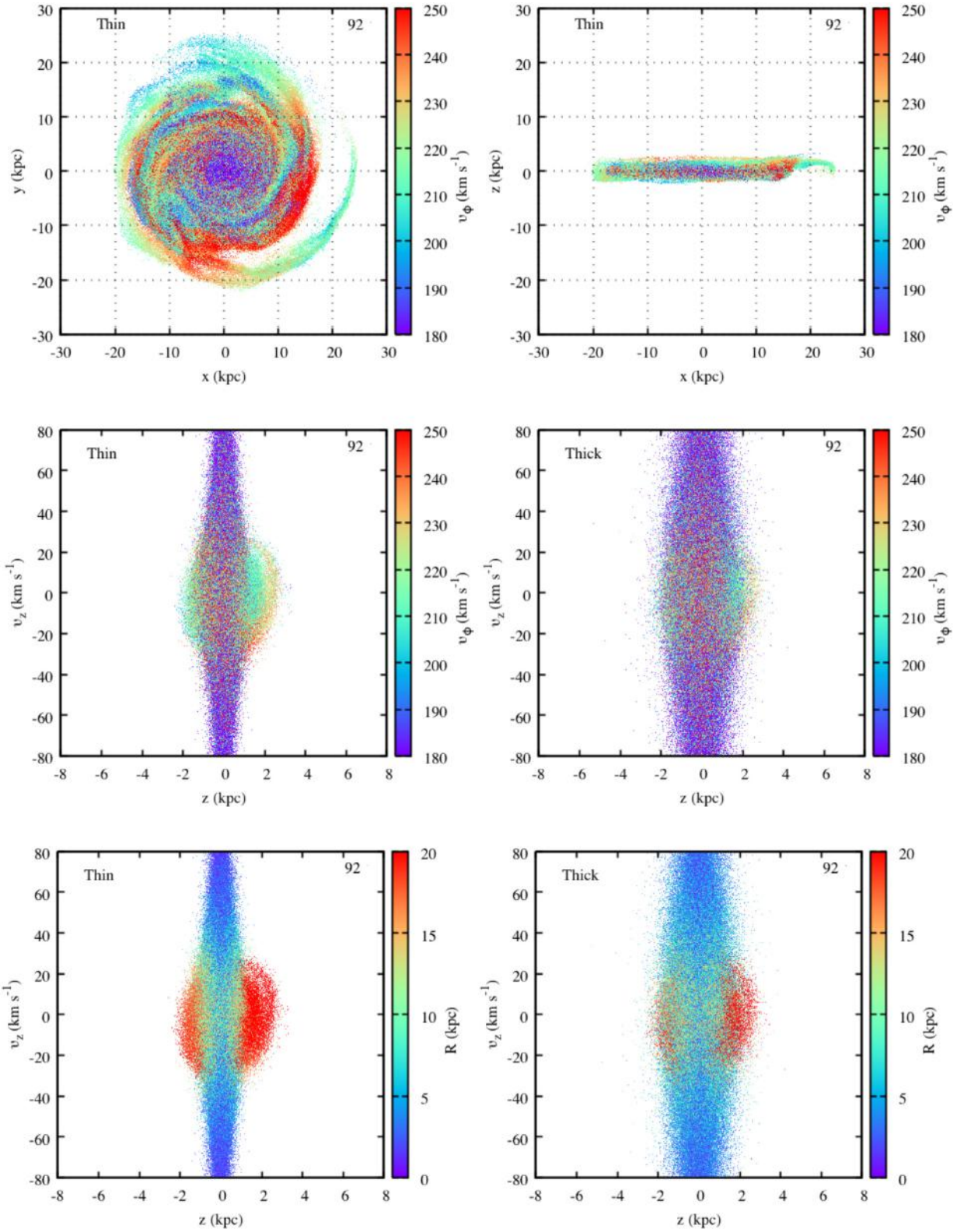

Figure 23. Simulation of an intermediate-mass intruder (Model S; Table 2) on a hyperbolic orbit where only the Galaxy is shown. (a) *xy* plane for the thin disc where the particles are colour coded with V_ϕ (Movie S2). (b) *xz* plane for the thin disc where the particles are colour coded with V_ϕ (Movie S2). (c) zV_z phase plane for the thin disc colour coded with V_ϕ (Movie S3). (d) zV_z phase plane for the thick disc colour coded with V_ϕ (Movie S3). (e) zV_z phase plane for the thin disc colour coded with R (Movie S4). (f) zV_z phase plane for the thick disc colour coded with R (Movie S4). Once again, there are coherent velocity structures across all phase planes ($t = 92$ Myr). Now the physical and kinematic extent have both declined by almost a factor of two, consistent with the lower intruder mass. In (e), the one-armed phase spiral at 20 kpc is still apparent. The inner phase spiral pattern at $R = 10$ kpc is no longer visible.

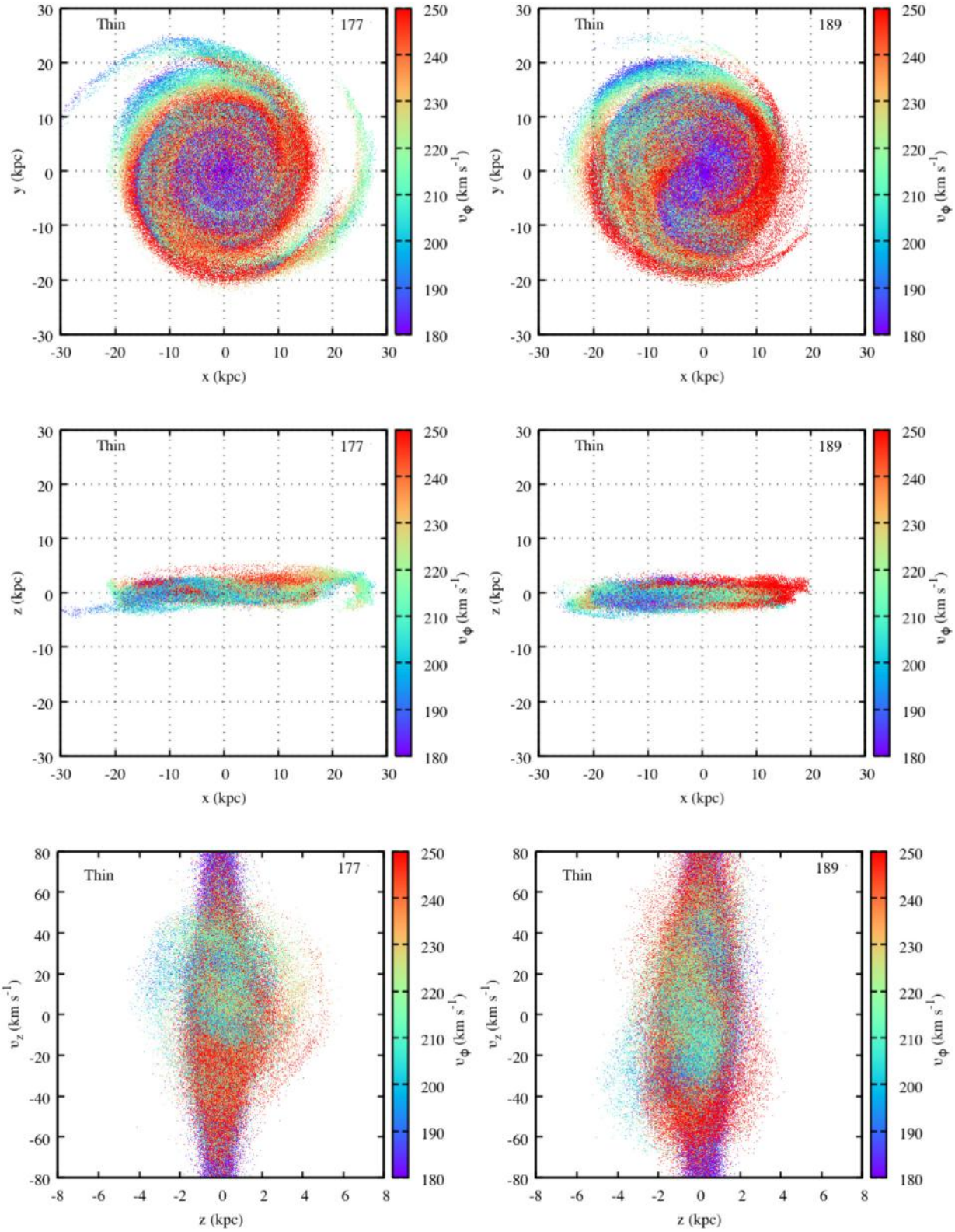

Figure 24. Simulation of a high-mass intruder (Model K; Table 2) on a realistic Sgr orbit where only the Galaxy is shown. We present results for just before and just after the last disc transit which occurred at 1.8 Gyr in the simulation. (a) *xy* plane for the thin disc 30 Myr *before* transit where the particles are colour coded with V_ϕ. (b) Same as in (a), but 90 Myr *after* the disc crossing. (c) *xz* plane for the thin disc 30 Myr *before* transit where the particles are colour coded with V_ϕ. (d) Same as in (c), but 90 Myr *after* the disc crossing. (e) zV_z plane 30 Myr *before* the disc crossing. (f) Same as (e), but 90 Myr *after* the disc crossing. Note how the coherent phase-space structures in (e) are wiped out in (f); the extent in z is also compressed right after the disc transit such that the pattern must rebuild from scratch. Weaker related one-armed structures are seen in $V_R(z, V_z)$ as we observe in the accompanying simulations (Movie K5; Table 5).

that what we observe today *cannot* be older than the lookback time of the last disc crossing.

8.4 Future research

Natural directions for future work include using the distributions of α-rich and α-poor stars in action space shown in Fig. 4 to build extended distribution functions (EDF) for the discs (Sanders & Binney 2015), and use these EDFs to construct a self-consistent model Galaxy. Such a model would predict the density and kinematics of the two discs throughout the Galaxy, and thus provide a link to other spectroscopic surveys that can separate the discs at other locations. While the Galaxy is not in equilibrium, the work of Binney & Schönrich (2018) shows the value of such models as frameworks within which to model non-equilibrium features such as the phase spiral.

The wealth of evidence that we now have, that the disc near us is vertically excited, and the strong suspicion that the Sgr dwarf (which was discovered 30 yr after the HI warp!) is the prime cause of this excitation, suggests that it is time to develop definitive models of both the warp and the dwarf's orbit. It seems likely that this will be achieved through meticulous and innovative *N*-body modelling. This work is of direct relevance to our understanding of the nature of dark matter. If satisfactory models can be achieved, they must surely provide conclusive evidence that dark matter, which is dominant in the regions of interest, absorbs energy and momentum from moving massive bodies like ordinary matter. Then, we would have conclusive evidence that dark matter comprises non-degenerate fermions (Bœhm & Fayet 2004) rather than being an artefact introduced by using the wrong theory of gravity (Milgrom & Sanders 2008) or being a bosonic condensate of an ultralight quantum field (q.v. Hui et al. 2017).

ACKNOWLEDGEMENTS

This work has made use of data from the ESA mission *Gaia* (https://www.cosmos.esa.int/gaia), processed by the *Gaia* Data Processing and Analysis Consortium (https://www.cosmos.esa.int/web/gaia/dpac/consortium). This work is also based on data acquired from the Australian Astronomical Telescope. We acknowledge the traditional owners of the land on which the AAT stands, the Gamilaraay people, and pay our respects to elders past and present.

JBH is supported by an ARC Australian Laureate Fellowship (FL140100278) and the ARC Centre of Excellence for All Sky Astrophysics in 3 Dimensions (ASTRO-3D) through project number CE170100013. SS is funded by a Dean's University Fellowship and through JBH's Laureate Fellowship, which also supports TTG and GDS. MJH is supported by an ASTRO-3D Fellowship. JK is supported by a Discovery Project grant from the Australian Research Council (DP150104667) awarded to JBH. JJB is supported by the UK Science and Technology Facilities Council under grant number ST/N000919/1.

SB and KL acknowledge funds from the Alexander von Humboldt Foundation in the framework of the Sofja Kovalevskaja Award endowed by the Federal Ministry of Education and Research. SB, MA, and KL acknowledge travel support from Universities Australia and Deutsche Akademische Austauschdienst. The research by MA, LD, JL, and AMA has been supported by an Australian Research Council Laureate Fellowship to MA (grant FL110100012). LD gratefully acknowledges a scholarship from Zonta International District 24 and support from ARC grant DP160103747. LD, KF, and YST are grateful for support from Australian Research Council grant DP160103747. KL acknowledges funds from the Swedish Research Council (Grant no. 2015-00415_3) and Marie Sklodowska Curie Actions (Cofund Project INCA 600398). SLM acknowledges support from the Australian Research Council through grant DE140100598. TZ acknowledges the financial support from the Slovenian Research Agency (research core funding no. P1-0188). YST is supported by the Carnegie-Princeton Fellowship, the Chooljian Membership from the Institute for Advanced Study in Princeton and the NASA Hubble Fellowship grant HST-HF2-51425.001 awarded by the Space Telescope Science Institute.

JBH and TTG acknowledge the Sydney Informatics Hub and the University of Sydney's high-performance computing (HPC) cluster Artemis for providing the HPC resources that have contributed to the some of the research results reported within this paper. Parts of this project were undertaken with the assistance of resources and services from the National Computational Infrastructure (NCI), which is supported by the Australian Government.

We acknowledge constructive conversations with Jerry Sellwood, Elena d'Onghia, Ralph Schönrich, Evgeny Vasiliev, Kathryn Johnston, Ivan Minchev, and Chervin Laporte. We thank Nick Prantzos at the Shanghai Galactic Archaeology meeting (2018 November) for promoting the need for improved nomenclature across the different [α/Fe] components, Sten Hasselquist for showing us new data ahead of publication, and Lars Hernquist for suggesting the compact α notation in an open discussion with the GALAH team held at the University of Sydney. We are also indebted to a persistent and insightful referee.

REFERENCES

Adibekyan V. Z., Sousa S. G., Santos N. C., Delgado Mena E., González Hernández J. I., Israelian G., Mayor M., Khachatryan G., 2012, A&A, 545, A32
Antoja T. et al., 2018, Nature, 561, 360
Aumer M., Binney J., Schönrich R., 2016, MNRAS, 462, 1697
Barden S. C. et al., 2010, Proc. SPIE, 7735, 773509
Bensby T., Alves-Brito A., Oey M. S., Yong D., Meléndez J., 2011, ApJ, 735, L46
Bensby T., Feltzing S., Lundström I., 2003, A&A, 410, 527
Bensby T., Feltzing S., Oey M. S., 2014, A&A, 562, A71
Bergemann M. et al., 2018, Nature, 555, 334
Binney J., Jiang I.-G., Dutta S., 1998, MNRAS, 297, 1237
Binney J., Schönrich R., 2018, MNRAS, 481, 1501
Binney J., Tremaine S., 2008, Galactic Dynamics, 2nd edn. Princeton Univ. Press, Princeton, NJ
Binney J. et al., 2014, MNRAS, 439, 1231
Bland-Hawthorn J., Gerhard O., 2016, ARA&A, 54, 529
Bland-Hawthorn J., Kos J., Betters C. H., De Silva G., O'Byrne J., Patterson R., Leon-Saval S. G., 2017, Opt. Exp., 25, 15614
Bland-Hawthorn J., Krumholz M. R., Freeman K., 2010, ApJ, 713, 166
Bovy J., 2015, ApJS, 216, 29
Brunetti M., Chiappini C., Pfenniger D., 2011, A&A, 534, A75
Buder S. et al., 2018, MNRAS, 478, 4513
Bœhm C., Fayet P., 2004, Nucl. Phys. B, 683, 219
Candlish G. N., Smith R., Fellhauer M., Gibson B. K., Kroupa P., Assmann P., 2014, MNRAS, 437, 3702
Carlin J. L. et al., 2013, ApJ, 777, L5
Chiappini C., Matteucci F., Romano D., 2001, ApJ, 554, 1044
Daniel K. J., Wyse R. F. G., 2015, MNRAS, 447, 3576
Daniel K. J., Wyse R. F. G., 2018, MNRAS, 476, 1561
Dehnen W., 1998, AJ, 115, 2384
de la Vega A., Quillen A. C., Carlin J. L., Chakrabarti S., D'Onghia E., 2015, MNRAS, 454, 933
Deng L.-C. et al., 2012, Res. Astron. Astrophys., 12, 735

De Silva G. M. et al., 2015, MNRAS, 449, 2604
Elmegreen B. G., Sundin M., Kaufman M., Brinks E., Elmegreen D. M., 1995, ApJ, 453, 139
Famaey B., Jorissen A., Luri X., Mayor M., Udry S., Dejonghe H., Turon C., 2005, A&A, 430, 165
Fouvry J.-B., Pichon C., Chavanis P.-H., Monk L., 2017, MNRAS, 471, 2642
Fouvry J. B., Pichon C., Magorrian J., Chavanis P. H., 2015, A&A, 584, A129
Freeman K., Bland-Hawthorn J., 2002, ARA&A, 40, 487
Freeman K., Bland-Hawthorn J., 2008, in Kodama T., Yamada T., Aoki K., eds, ASP Conf. Ser. Vol. 399, Panoramic Views of Galaxy Formation and Evolution. Astron. Soc. Pac., San Francisco, p. 439
Fuhrmann K., 1998, A&A, 338, 161
Gaia Collaboration et al., 2018a, A&A, preprint (arXiv:1804.09382)
Gaia Collaboration et al., 2018b, A&A, 616, A1
Gaia Collaboration et al., 2018c, A&A, 616, A10
Gaia Collaboration et al., 2018d, A&A, 616, A12
Gilmore G., Reid N., 1983, MNRAS, 202, 1025
Gilmore G. et al., 2012, The Messenger, 147, 25
Goldreich P., Lynden-Bell D., 1965, MNRAS, 130, 125
Gravity Collaboration et al., 2018, A&A, 615, L15
Guiglion G. et al., 2015, A&A, 583, A91
Gómez F. A., Besla G., Carpintero D. D., Villalobos Á., O'Shea B. W., Bell E. F., 2015, ApJ, 802, 128
Gómez F. A., Minchev I., O'Shea B. W., Beers T. C., Bullock J. S., Purcell C. W., 2013, MNRAS, 429, 159
Hasselquist S. et al., 2017, ApJ, 845, 162
Hasselquist S. et al., 2019, ApJ, accepted (astroph/1901.04559)
Hawkins K., Jofré P., Masseron T., Gilmore G., 2015, MNRAS, 453, 758
Hayden M. R., Recio-Blanco A., de Laverny P., Mikolaitis S., Worley C. C., 2017, A&A, 608, L1
Hayden M. R. et al., 2015, ApJ, 808, 132
Hayden M. R. et al., 2019, MNRAS, submitted (arXiv:1901.07565)
Haywood M., Di Matteo P., Lehnert M. D., Katz D., Gómez A., 2013, A&A, 560, A109
Hernquist L., 1990, ApJ, 356, 359
Hui L., Ostriker J. P., Tremaine S., Witten E., 2017, Phys. Rev. D, 95, 043541
Hunter C., Toomre A., 1969, ApJ, 155, 747
Ibata R. A., Wyse R. F. G., Gilmore G., Irwin M. J., Suntzeff N. B., 1997, AJ, 113, 634
Jiang I.-G., Binney J., 2000, MNRAS, 314, 468
Jordi C. et al., 2010, A&A, 523, A48
Jílková L., Carraro G., Jungwiert B., Minchev I., 2012, A&A, 541, A64
Kalberla P. M. W., Kerp J., 2009, ARA&A, 47, 27
Kos J. et al., 2017, MNRAS, 464, 1259
Kos J. et al., 2018a, MNRAS, 480, 5242
Kos J. et al., 2018b, MNRAS, 480, 5475
Laporte C. F. P., Minchev I., Johnston K. V., Gómez F. A., 2019, MNRAS, submitted (arXiv:1808.00451)
Law D. R., Johnston K. V., Majewski S. R., 2005, ApJ, 619, 807
Li T. S. et al., 2017, ApJ, 844, 74
Lockman F. J., 2002, in Taylor A. R., Landecker T. L., Willis A. G., eds, ASP Conf. Ser. Vol. 276, Seeing Through the Dust: The Detection of HI and the Exploration of the ISM in Galaxies. Astron. Soc. Pac., San Francisco, p. 107
Lynden-Bell D., 1967, MNRAS, 136, 101
Majewski S. R. et al., 2017, AJ, 154, 94
Martell S. L. et al., 2017, MNRAS, 465, 3203
Masseron T., Gilmore G., 2015, MNRAS, 453, 1855
Masset F., Tagger M., 1997, A&A, 322, 442
Matthews L. D., Uson J. M., 2008a, AJ, 135, 291
Matthews L. D., Uson J. M., 2008b, ApJ, 688, 237
McMillan P. J., 2011, MNRAS, 414, 2446
Milgrom M., Sanders R. H., 2008, ApJ, 678, 131
Minchev I., Famaey B., 2010, ApJ, 722, 112
Minchev I., Famaey B., Combes F., Di Matteo P., Mouhcine M., Wozniak H., 2011, A&A, 527, A147
Minchev I. et al., 2018, MNRAS, 481, 1645
Miyamoto M., Nagai R., 1975, PASJ, 27, 533
Newberg H. J., Yanny B., Cole N., Beers T. C., Re Fiorentin P., Schneider D. P., Wilhelm R., 2007, ApJ, 668, 221
Newberg H. J. et al., 2002, ApJ, 569, 245
Nieva M.-F., Przybilla N., 2012, A&A, 539, A143
Perret V., Renaud F., Epinat B., Amram P., Bournaud F., Contini T., Teyssier R., Lambert J.-C., 2014, A&A, 562, A1
Perryman M. A. C. et al., 2001, A&A, 369, 339
Piffl T. et al., 2014, MNRAS, 445, 3133
Posti L., Helmi A., Veljanoski J., Breddels M. A., 2018, A&A, 615, A70
Prusti T. et al., 2016, A&A, 595, A1
Purcell C. W., Bullock J. S., Tollerud E. J., Rocha M., Chakrabarti S., 2011, Nature, 477, 301
Quillen A. C., Minchev I., Bland-Hawthorn J., Haywood M., 2009, MNRAS, 397, 1599
Quillen A. C., Nolting E., Minchev I., De Silva G., Chiappini C., 2018, MNRAS, 475, 4450
Reid M. J., Brunthaler A., 2004, ApJ, 616, 872
Rocha-Pinto H. J., Majewski S. R., Skrutskie M. F., Crane J. D., Patterson R. J., 2004, ApJ, 615, 732
Roškar R., Debattista V. P., Quinn T. R., Wadsley J., 2012, MNRAS, 426, 2089
Russell S. C., Dopita M. A., 1992, ApJ, 384, 508
Sanders J. L., Binney J., 2015, MNRAS, 449, 3479
Schönrich R., Binney J., 2009, MNRAS, 396, 203
Schönrich R., Binney J., Dehnen W., 2010, MNRAS, 403, 1829
Schönrich R., Dehnen W., 2018, MNRAS, 478, 3809
Schönrich R., McMillan P. J., 2017, MNRAS, 467, 1154
Sellwood J. A., Binney J. J., 2002, MNRAS, 336, 785
Sellwood J. A., Carlberg R. G., 2014, ApJ, 785, 137
Sharma S., 2017, ARA&A, 55, 213
Sharma S., Bland-Hawthorn J., Johnston K. V., Binney J., 2011, ApJ, 730, 3
Sharma S. et al., 2014, ApJ, 793, 51
Sharma S. et al., 2018, MNRAS, 473, 2004
Sheinis A. et al., 2015, J. Astron.Telesc. Instrum. Syst., 1, 035002
Siebert A. et al., 2008, MNRAS, 391, 793
Slater C. T. et al., 2014, ApJ, 791, 9
Sofia U. J., Meyer D. M., 2001, ApJ, 554, L221
Solway M., Sellwood J. A., Schönrich R., 2012, MNRAS, 422, 1363
Spagna A., Lattanzi M. G., Re Fiorentin P., Smart R. L., 2010, A&A, 510, L4
Springel V., Di Matteo T., Hernquist L., 2005, MNRAS, 361, 776
Steinmetz M. et al., 2006, AJ, 132, 1645
Tepper-García T., Bland-Hawthorn J., 2018, MNRAS, 478, 5263
Teyssier R., 2002, A&A, 385, 337
Toomre A., 1964, ApJ, 139, 1217
Toomre A., 1969, ApJ, 158, 899
Toomre A., 1981, in Fall S. M., Lynden-Bell D., eds, Structure and Evolution of Normal Galaxies. Cambridge Univ. Press, Cambridge, p. 111
Vasiliev E., 2018, Astrophysics Source Code Library, record ascl:1805.008
Vera-Ciro C., D'Onghia E., Navarro J., Abadi M., 2014, ApJ, 794, 173
Widrow L. M., Gardner S., Yanny B., Dodelson S., Chen H.-Y., 2012, ApJ, 750, L41
Williams M. E. K. et al., 2013, MNRAS, 436, 101
Wittenmyer R. A. et al., 2018, AJ, 155, 84
Xu Y., Newberg H. J., Carlin J. L., Liu C., Deng L., Li J., Schönrich R., Yanny B., 2015, ApJ, 801, 105
Yanny B., Gardner S., 2013, ApJ, 777, 91
Zari E., Hashemi H., Brown A. G. A., Jardine K., de Zeeuw P. T., 2018, A&A, 620, A172
Zwitter T. et al., 2018, MNRAS, 481, 645

APPENDIX A: MOVIES

A1 Reference model: isolated Galaxy

In Movie P1,[6] we witness the long-term evolution of the isolated Galaxy model (Model P) summarized in Table 1. The frames are shown with time steps of $\Delta t = 10$ Myr that are short enough to trace most stellar orbits reliably. The disc settles to an equilibrium configuration within a few hundred Myr. This can be seen from the settling to a cold, thin disc in the edge-on and face-on projections, with a constant vertical scale height. The disc generates low-level flocculent (transient) spiral perturbations consistent with the intrinsic numerical and spatial resolutions, but individual stellar orbits confirm that the coarse-grained potential is well behaved. The simulation includes a thick disc which is shown only in the vertical phase plane. Since the thick disc is older and more metal poor than the thin disc, including two discs allows us to study the predicted age and metallicity dependence of the cohent spiral. This is the base model we use to study the perturbation induced by an intruder.

In Movie P2, we show the same configuration space for Movie P1, but now each star is colour-coded by its azimuthal velocity V_ϕ in the plane of the disc. The velocity field reflects the underlying rotation curve consistent with the total gravitational potential. This becomes relevant when comparing to the perturbed cases below. There are small variations across the disc consistent with the stochastic spiral perturbations.

In Movie P3, the evolution of the thin and thick discs is shown in the vertical phase plane (z, V_z) coded by the azimuthal velocity V_ϕ, i.e. $V_\phi(z, V_z)$. There is no statistical averaging $\langle V_\phi \rangle$ over the population as carried out for the *Gaia* data (e.g. Fig. 6). These are projections of the *entire* disc population except that we have removed all points inside of $R = 5$ kpc. Otherwise, the phase plane would be dominated by the inner disc with its higher V_z motions compressed in z. The different vertical thicknesses are evident and they remain fairly constant as the disc evolves. Each star moves clockwise around $(z, V_z) = (0,0)$ as it oscillates in the disc potential with an angular frequency Ω_z. No coherent patterns emerge because the phases are randomized over 2π.

In Movie P4, we show the evolution of the thin and thick discs in the vertical phase plane (z, V_z) coded by the radial distance R, i.e. $R(z, V_z)$. No significant structural evolution is evident once the disc has settled.

A2 Perturbed model: hyperbolic orbit

Movies T1, S1, and R1 show the interaction of the Galaxy with the low-, intermediate-, and high-mass intruders respectively, each on a hyperbolic orbit (shown as a filled red circle) crossing the disc at about $R = 13$ kpc. At $t \sim 95$ Myr, the disc moves up towards the approaching intruder and its centre of mass experiences a recoil. By the time the intruder has transited the disc plane, the entire disc has responded to the perturber. By $t = 180$ Myr, the interaction has excited a spiral arm and a strong warp in the outer disc that precesses in the plane around the centre of mass (cf. Gómez et al. 2015). The upwards momentum of the disc does not reverse until after $t = 400$ Myr. The strong forcing by the perturber is active for less than 100 Myr but the disc response persists for the 2 Gyr duration of the movie. For reference, the results are also shown in Figs 22 and 23 respectively at a single time-step ($t = 900$ Myr).

[6] http://www.physics.usyd.edu.au/galah_exp/sp

In Figs 22 (R2) and 23 (S2), when compared to the isolated Galaxy model (Movie P2), the azimuthal velocity field V_ϕ shows systematic variations due to the low-amplitude bending waves (corrugations or wrinkles) propagating through the disc. The kinematically distinct, azimuthal 'plumes' (confined in radius) arise from disc segments displaced vertically by varying amounts, with larger displacements resulting in bigger lags with respect to the disc rotation at that radius. In other words, these kinematic plumes are mostly associated with large V_z motion and some V_R motion.

In Figs 22 (R3) and 23 (S3), these same kinematic plumes encoded with the same V_ϕ velocities manifest in the (z, V_z) plane. In Figs 22 (R4) and 23 (S4) using the $R(z, V_z)$ plane, we show plumes at two different radii for a single time-step ($t = 900$ Myr). The spiral feature at 10 kpc aligns and elongates with the disc, whereas the feature in the outer disc appears more circular as expected from theory (Fig. 20). In the absence of another disc-transiting event, these spiral features can be long-lived ($\gtrsim 500$ Myr) in the vertical phase plane.

There is only a finite number of kinematic plumes in the zV_z plane because the corrugations have a long wavelength of order several kiloparsecs, as observed in the Galaxy (Xu et al. 2015) and in external galaxies (Matthews & Uson 2008b), and expected from theory (Masset & Tagger 1997). The aspect ratio in zV_z space, the degree of winding up and the total amplitude depend on the disc location (Fig. 20).

At times, a one-armed spiral feature is clear (e.g. Movies S3 and R3 during $1.2 < t < 1.9$ Gyr) although tracing it to the origin in (z, V_z) proves to be difficult without the action analysis (Section 4.3) applied directly to the models (Tepper-García et al. in preparation). This is because our sampling (limited by N_P) is not sufficient to provide contrast against the clockwise population from the dominant underlying disc.

In Fig. 22, for the high-mass intruder (R3), there are several coherent one-armed plumes in the (z, V_z) plane. Once again, these grow to their maximum amplitude in $|z_{max}| \approx 6$ kpc and $|V_{z_{max}}| \approx 60$ km s^{-1} long after the transit has occurred. This appears to be associated with the strong vertical recoil of the disc after its reversal along the intruder's orbit. In particular, note the coherent *elliptic* plume aligned with and encircling the disc ($V_z < 0$) emerging at $t = 900$ Myr and persisting for 100 Myr. The elongation in V_z compared to z (Fig. 20) reinforces that this feature occurs at smaller radius ($R \approx 13-15$ kpc). There are spiral plumes down to maybe $R \approx 10$ kpc but insufficiently populated to give good contrast. This is a failing of the current models. Much larger simulations with an order of magnitude more particles are already under way.

In Fig. 23, for the intermediate-mass intruder (S3), we see the kinematic spiral has lower amplitude in both axes. It grows out of the disc, rotates as a fixed pattern, reaching its maximum amplitude in $|z_{max}| \approx 2.5$–3 kpc and $|V_{z_{max}}| \approx 30$–40 km s^{-1}. In Fig. 23 (S4), the vertical phase plane is encoded with the Galactocentric radius R: we see that the coherent spiral patterns occur at $R \approx 15-20$ kpc. (These features may also be associated with the reversal of the disc's momentum parallel to the intruder's orbit.) We note that $|z_{max}|$ and $|V_{z_{max}}|$ approximately match the predicted values in Fig. 20 at $R = 20$ kpc; the model effectively 'calibrates' the expected amplitudes at other radii, in particular the anticipated values of $|z_{max}| \approx 1$ kpc and $|V_{z_{max}}| \approx 50$ km s^{-1} at $R \approx R_0$ (Antoja et al. 2018). We see the effects of the phase spiral at lower radii down to 10 kpc but the contrast is poor.

In Fig. 22 (R4), the strongest phase spiral signal is further out at $R \approx 20$ kpc. The outer disc of the Galaxy must be experiencing a strong forced oscillation, with stars confined to well-defined

corrugations or wrinkles (Schönrich & Dehnen 2018). This is a strong prediction of our simulations given the low-flying orbit of Sgr over the disc. It seems reasonable to consider that this is the explanation for the TriAndromeda and Monoceros 'rings' discovered by the SDSS survey towards the outer stellar disc (Xu et al. 2015; Li et al. 2017) and maybe even most of the wave-like structure, ripples and corrugations claimed to date (Schönrich & Dehnen 2018; Bergemann et al. 2018).

A3 Perturbed model: realistic orbit

In Movie M1 (footnote 6), we present our model for the low-mass Sgr impact along a realistic orbit (see Tepper-García & Bland-Hawthorn 2018). Contemporary models agree that Sgr initially crossed the disc along a trajectory perpendicular to the Galactic plane (e.g. Law et al. 2005; Purcell et al. 2011). But at late times, as the orbit became circularized by dynamical friction (e.g. Jiang & Binney 2000), the trajectory evolved to be more inclined to the disc ($i \lesssim 30^\circ$), and therefore less impulsive. The last crossing occurred at a radius of about $R \approx 13$ kpc.

All of the movies from Model M look very similar to the unperturbed case (Model P), with the exception of one. When we compare model M3 to the stable model P3 for the thin disc, there is clear evidence of heating in the former due to the action of the low-mass perturber. Such dynamical heating can happen over the disc where the forcing frequency is out of phase with the intrinsic disc response. This heating also occurs in the high- and intermediate-mass cases but this is obscured by the dramatic plumes arising from the disc.

In Movies L and K (footnote 6), we present our model for the intermediate- and high-mass impacts respectively along essentially the same orbit. In Fig. 24, we show frames from Movie K4 at two different time-steps, 30 Myr before and 90 Myr after a disc transit. This is to emphasize how clean the phase spiral signature is right before impact, and how it is wiped out for up to ≈100−150 Myr after the impact, reforming thereafter.

In Fig. 24(e), there are three distinct phase spiral patterns arising in three radial bins ($R = 17$, 15, and 12 kpc). We can calibrate the strength of the signal in Antoja et al. (2018) from our numerical simulations, confirmed by the single crossing hyperbolic models. The low-mass intruder (Model M) barely ruffles the disc. The high-mass intruder (Model K) produces features with $|z_{\rm max}| \lesssim 5$ kpc and $|V_{z_{\rm max}}| \lesssim 50$ km s $^{-1}$, comparable to the results for the high-mass hyperbolic case (Model R). The intermediate-mass case scales down as it did for the hyperbolic models, thus consistent with the amplitude of the Antoja spiral at $R = R_0$.

After impact, the spiral features arise again from the ashes and are persistent until the next impact. The fact that we see a clear phase spiral today is consistent with the passage of time since the last crossing about 400−500 Myr ago (by general consensus) and our imminent disc crossing in $\gtrsim$50 Myr. This makes the spiral phenomenon no older than ∼0.5 Gyr.

[1]*Sydney Institute for Astronomy, School of Physics, A28, The University of Sydney, NSW 2006, Australia*
[2]*Center of Excellence for Astrophysics in Three Dimensions (ASTRO-3D), Australia*
[3]*Miller Institute, University of California Berkeley, CA 94720, USA*
[4]*Rudolf Peierls Centre for Theoretical Physics, Clarendon Laboratory, Oxford OX1 3PU, UK*
[5]*Research School of Astronomy and Astrophysics, Australian National University, ACT 2611, Australia*
[6]*Department of Physics and Astronomy, Macquarie University, Sydney, NSW 2109, Australia*
[7]*Max Planck Institute for Astronomy (MPIA), Koenigstuhl 17, D-69117 Heidelberg, Germany*
[8]*International Max Planck Research School for Astronomy and Cosmic Physics, University of Heidelberg, Germany*
[9]*Monash Centre for Astrophysics, Monash University, VIC 3800, Australia*
[10]*School of Physics and Astronomy, Monash University, VIC 3800, Australia*
[11]*INAF Astronomical Observatory of Padova, I-36012 Asiago, Italy*
[12]*Department of Physics and Astronomy, Uppsala University, Box 516, SE-751 20 Uppsala, Sweden*
[13]*School of Physics, UNSW, Sydney, NSW 2052, Australia*
[14]*Department of Astronomy, Columbia University, Pupin Physics Laboratories, New York, NY 10027, USA*
[15]*Center for Computational Astrophysics, Flatiron Institute, 162 Fifth Avenue, New York, NY 10010, USA*
[16]*Faculty of Mathematics and Physics, University of Ljubljana, Jadranska 19, 1000 Ljubljana, Slovenia*
[17]*ICRAR, The University of Western Australia, 35 Stirling Highway, Crawley, WA 6009, Australia*
[18]*Department of Physics and Astronomy, University of Rochester, Rochester, NY 14627, USA*
[19]*Institute for Advanced Study, Princeton, NJ 08540, USA*
[20]*Department of Astrophysical Sciences, Princeton University, Princeton, NJ 08544, USA*
[21]*Observatories of the Carnegie Institution of Washington, 813 Santa Barbara Street, Pasadena, CA 91101, USA*
[22]*Department of Physics and Astronomy, The Johns Hopkins University, Baltimore, MD 21218, USA*

This paper has been typeset from a TEX/LATEX file prepared by the author.